Soft Matter

Accepted Manuscript

This article can be cited before page numbers have been issued, to do this please use: M. Asgari, *Soft Matter*, 2017, DOI: 10.1039/C7SM00911A.

ROYAL SOCIETY OF CHEMISTRY

rsc.li/soft-matter-journal

View Article Online
DOI: 10.1039/C7SM00911A

Journal Name

ARTICLE TYPE

Cite this: DOI: 10.1039/xxxxxxxxxx

Micro-mechanical, continuum-mechanical, and AFM-based descriptions of elasticity in open cylindrical micellar filaments

Meisam Asgari*

Received Date
Accepted Date

DOI: 10.1039/xxxxxxxxxx

www.rsc.org/journalname

We present theoretical and experimental descriptions of the elasticity of cylindrical micellar filaments using micro-mechanical and continuum theories, and Atomic Force Microscopy. Following our micro-mechanical elasticity model for micellar filaments [Asgari, *Eur. Phys. J. E* 2015, **38(9)**], the elastic bending energy of hemispherical end caps is found. The continuum description of the elastic bending energy of a cylindrical micellar filament is also derived using constrained Cosserat rod theory. While the continuum approach provides macroscopic description of the strain energy of the micellar filament, the micro-mechanical approach has a microscopic view of the filament, and provides expressions for kinetic variables based on a selected interaction potential between the molecules comprising the filament. Our model predicts the dependence of the elastic modulus of the micellar filaments on their diameter, which agrees with previous experimental observations. Atomic force microscopy is applied to estimate the elastic modulus of the filaments using force volume analysis. The obtained values of elastic modulus yield the persistence length of micellar filaments on the same order of the previously reported values. Consistent with previous studies, our results indicate that semi-flexible linear micelles have a relatively large local strain energy at their end points, which explains their tendency to fuse to minimize the number of end caps at relatively low total surfactant volume fractions. Also, the elastic modulus of micellar filaments was found to increase when the indentation frequency increases, a finding which agrees with previous rheological observations on the bulk shear modulus of micellar solutions.

1 Introduction

Surfactants are amphiphiles composed of two parts: a long hydrophobic tail, and a hydrophilic head group with a high affinity with water. In aqueous solutions of different concentrations, these amphiphiles self-assemble reversibly into a variety of spatially organized structures such as spherical micelles, cylindrical micellar filaments, disk micelles, toroidal micelles, hexagonal liquid crystals, lamellar liquid crystals, and vesicles, in all of which the hydrophobic tails tend to avoid contact with water.[1–12] A spherical micelle may grow into short cylindrical micellar filaments.[4,9,13] The ends of a cylindrical micellar filament are assumed to be capped by identical hemispheres.[14] Adding more amphiphiles to the solution at certain temperatures may cause the formation of long, branched or unbranched, cylindrical micellar filaments often called wormlike micelles.[15–18] According to Oelschlaeger *et al.*[11] and Cates and Candau,[3] if the sufficient energy for creating two hemispherical end caps from a very long micellar filament is relatively large and the solution is sufficiently dilute, short micellar filaments might merge to reduce the number of end caps.

Cylindrical micellar filaments are often modeled as spherocylinders, comprised of a relatively long cylindrical body, capped by two hemispheres at their ends whose radii are assumed to be equal to that of the cylindrical middle part.[19,20] Such micelles are mostly characterized by their persistence length, which can be obtained from bending free energy.[21–24] Thus, the concept of elastic free-energy plays an important role in studying these nanostructures.

It is widely accepted that bending elasticity of self-assembled aggregates plays a crucial role in describing their mechanical behaviour and equilibrium configurations. May *et al.*[16] considered the extent to which the bending elasticity of cylindrical micellar filaments influences their tendency to join and form branched structures. In their work, the free-energy density of a cylindrical micelle is comprised of the chain conformational energy, the end cap contribution, and the hydrocarbon-water interfacial en-

---

* *Department of Mechanical Engineering, McGill University, 817 Sherbrooke street west, Montreal, QC H3A 0C3, Canada; E-mail: meisam.asgari@mail.mcgill.ca*

View Article Online
DOI: 10.1039/C7SM00911A

ergy. Their findings indicate that the energy change associated with the formation of a junction between one micellar end cap and the cylindrical body of another micelle is small relative to the elastic bending energy of an end cap.[16]

A useful tool to quantitatively describe the bending properties of self-assembled aggregates has been the Canham–Helfrich elastic bending energy density—the elastic bending energy per unit area at a point on the surface of an aggregate—that was originally developed for a lipid vesicle, and can be expressed mathematically as $\gamma_\circ + k_c(H-H_\circ)^2 + \bar{k}_c K$, where $\gamma_\circ$ denotes the interfacial stretching density known as the surface tension, H and K represent the mean and Gaussian curvatures of the surface, k_c and $\bar{k}_c$ are the splay and saddle-splay moduli, and $H_\circ$ is mean curvature of the natural, local shape of the lipid bilayer.[25–28] Whereas $\gamma_\circ$ shows the local stretching energy of the surface, the remaining two terms represent the bending free-energy of the interface at a constant area in the absence of stretching. The total elastic free energy of the aggregate is thus obtained by integrating the Canham–Helfrich elastic bending energy density over the surface area of the aggregate.

Micellar chains are treated as mesopolymers since they are subject to breaking and re-shaping.[30] They may also become entangled or form branched structures.[31] Similar to polymers, the persistence length $\langle l_p \rangle$ of a micellar chain is related to its bending rigidity k_c through $\langle l_p \rangle = k_c/2k_BT$, where $k_B = 1.38\times10^{-23}$ kgm^2/(s^{2}K) is Boltzmann's constant and T denotes the absolute temperature.[32–34] This characteristic length scale determines the energy cost of linear bending deformations in polymer chains and similar bio-filaments. The flexural rigidity k_c in the Canham–Helfrich elastic bending energy density carries the dimension of energy. According to the definition of persistence length of a polymer chain, the application of that term for cylindrical micellar filaments leaves a dimensionless value for persistence *length*. Considering this difficulty posed by the application of k_c in the definition of persistence length, and further, considering the large difference between the length and the cross-sectional dimensions of these nanostructures, an alternative approach might be to consider the energy density of an elastic rod, in which the bending rigidity carries the dimension of energy times length.[21,35]

Some prior investigations of micellar self-assembly have focused on using Canham–Helfrich elastic bending energy density for cylindrical micellar filaments.[36] However, on the basis of the mentioned similarity between micellar filaments and mesopolymers, existing expressions for the elastic bending energy density of a polymer chain provide some insight regarding the structure of the elastic bending energy density of a cylindrical micellar chain. Liu *et al.*[37] proposed an elastic bending energy density for a semi-flexible polymer chain with both bending and torsional elasticity of the form $k_1\kappa^2 + k_2(\tau-\tau_\circ)^2$, where k_1, k_2, and $\tau_\circ$ are respectively the flexural rigidity, torsional rigidity, and intrinsic torsion of the chain. Following the work of Kratky and Porod,[38] who took the configurational energy of a polymer chain to be a function of both the curvature and torsion of the chain, Bugl and Fujita[39] modeled a polymer chain as a continuous elastic homogeneous thin wire, using a slight extension, $k_1(\kappa-\kappa_\circ)^2 + k_2(\tau-\tau_\circ)^2$ that accounts for the potential importance of intrinsic curvature $\kappa_\circ$. More generally, Helfrich[40] derived an elastic bending energy density for a polymer chain that includes chiral effects, and is of the form $k_1\kappa^2 + k_2\kappa^2\tau + k_3\kappa^4 - k_4(\kappa'^2 + \kappa^2\tau^2)$, in which a prime denotes the derivative with respect to the arc-length, k_1 is the flexural rigidity, and k_2, k_3, and k_4 are other material parameters. Helfrich's energy density incorporates coupling between the curvature and the torsion of the curve representing the polymer chain. Helfrich's[40] derivation was purely geometrical and did not take into account the physics of the interactions between the building blocks of the polymer chain.

Recently, we derived an elastic bending energy density function for cylindrical micellar filaments based on the interactions between their constituent molecules.[21] In so doing, we treated the molecules comprising the micellar filament as one-dimensional rigid rods. The resulting function was found to contain a homogeneous contribution, as well as quadratic terms in curvature and torsion of the centreline of the micellar filament, as $\psi_\circ + k_c\kappa^2 + k_t\tau^2$. Here, we first review a synopsis of the calculation of the elastic bending energy density on the micellar body. We then apply the same methodology to obtain the elastic bending energy corresponding a hemispherical end cap in open cylindrical micellar filaments. Next, the continuum description of a cylindrical micellar filament is explored using constrained Cosserat rod theory.[43,44] We then apply Atomic force microscopy (AFM) to estimate the elastic modulus of the micellar filaments both on the micellar body and at the end caps.

The remainder of this article is planned as follows. Section 2 includes the details of the micro-mechanical model; in particular, the underlying assumptions are presented in 2.1, the necessary geometrical quantities, notation, and concepts are briefly presented in 2.2, and the synopsis of the calculation of the elastic bending energy density of the cylindrical body, and the detailed calculation of the end cap elastic bending energy are provided in 2.4 and 2.5. In Section 3, we use the constrained Cosserat rod model to find the continuum description of the elastic bending energy of a cylindrical micellar filament. The differences between the micro-mechanical and continuum models are discussed in Section 4. Details of the experiments such as sample preparations, AFM imaging, and force spectroscopy are presented in Section 5. The findings and implications of the study, and and propose directions for further research are discussed in Section 6. The conclusions appear in Section 7. A detailed account of the calculations of the elastic bending energy of the end caps is contained in the Appendix 9.1.

2 Micro-mechanical model

Our micro-mechanical model stems from the probabilistic and microscopic concepts of statistical mechanics. This approach enables us to extend the laws of thermodynamics to cases such as microscopic systems, which are not considered in classical thermodynamics. It further provides expressions for kinetic variables based on a selected interaction potential in combination with the ensemble properties. Here we apply this perspective to find the elastic bending energy of a cylindrical micellar filament, in terms of an arbitrary interaction potential between its constituent molecules. To do so, a set of meaningful simplifying assumptions

View Article Online
DOI: 10.1039/C7SM00911A

are essential.

2.1 Simplifying assumptions

As previously, we assume the amphiphiles forming the micellar filament to be physiochemically identical.[21] Each amphiphile is considered as a one-dimensional rigid rod with the length ξ.[21,47] Further, according to the observation that the hydrophobic tails of the molecules are oriented along the normal of the cylindrical interface,[16,48] the amphiphiles at any interior point of the centreline $\mathscr{C}$ are assumed to be perpendicular to $\mathscr{C}$ with a uniform angular distribution (see Figure 1). Hence, it is concluded that the spherical head-groups of amphiphiles lie on a cylindrical surface with a constant circular cross-section. In line with the new assumptions below, we model a cylindrical micellar chain as a cylindrical domain of a constant cross-sectional radius ξ, capped by two hemispheres of radius ξ at its ends. The centreline of such a domain is denoted by the curve $\mathscr{C}$ of length L.

(i) · Amphiphiles forming the end caps are distributed uniformly in the radial direction;

(ii) · End caps have the same number of amphiphiles;

(iii) · The length of a cylindrical micellar chain is larger than its radius (i.e., $L \gg \xi$). Thus, when the end caps are molded into their final shape, they are assumed to have the same radius as the cylindrical body.[42] Further, the maximum curvature that the micelle may exhibit at each point is denoted by $1/\ell$. The curve $\mathscr{C}$ is further assumed to be free of self-contact;

(iv) · The micelle is assumed to be symmetric with respect to rotation around its centreline $\mathscr{C}$, and also with respect to reflection through the plane perpendicular to $\mathscr{C}$ between the two end caps.

Items (i) and (ii) are simplifying assumptions for the arrangement of the molecules at the end caps. Assumption (iii) allows the filament to be identified with its centreline $\mathscr{C}$. It further ensures that the cylindrical body of the filament does not contact itself.

2.2 Geometry and Kinematics

In this section, the geometry of the micro-mechanical model for an open cylindrical micellar filament is introduced. Such a micelle possesses a cylindrical body capped by two hemispheres at its two ends. Hereafter, we consider a space curve $\mathscr{C} : s \to \boldsymbol{\chi}(s)$ representing the centreline of a cylindrical (or linear) micelle in Euclidean space $\mathbb{R}^3$, parametrized by arc-length s, with $0 \le s \le L$, where L is the total length of the centreline. Then, on using a superposed dot to denote differentiation with respect to arc-length s, the curvature κ and (the geometric) torsion τ of $\mathscr{C}$ are given by $\kappa = |\ddot{\boldsymbol{\chi}}(s)|$ and $\tau = \dot{\boldsymbol{\chi}}(s) \cdot (\ddot{\boldsymbol{\chi}}(s) \times \dddot{\boldsymbol{\chi}}(s))/|\ddot{\boldsymbol{\chi}}(s)|^2$. In general, the curve $\mathscr{C}$ is determined, up to a rigid translation, by these two locally invariant quantities. The unit tangent $\mathbf{t}$, unit normal $\mathbf{n}$, and unit binormal $\mathbf{b}$ of the Frenet frame $\{\mathbf{t},\mathbf{n},\mathbf{b}\}$ of $\mathscr{C}$ are given in terms of $\boldsymbol{\chi}(s)$ by $\mathbf{t}(s) = \dot{\boldsymbol{\chi}}(s)$, $\mathbf{n}(s) = \ddot{\boldsymbol{\chi}}(s)/|\ddot{\boldsymbol{\chi}}(s)|$, and $\mathbf{b}(s) = (\dot{\boldsymbol{\chi}}(s) \times \ddot{\boldsymbol{\chi}}(s))/|\ddot{\boldsymbol{\chi}}(s)|$. At a point with nonzero curvature, these three unit vectors are related through the coupled system of equations

$$\dot{\mathbf{t}} = \kappa\mathbf{n}, \quad \dot{\mathbf{n}} = -\kappa\mathbf{t} + \tau\mathbf{b}, \quad \& \quad \dot{\mathbf{b}} = -\tau\mathbf{n}, \tag{1}$$

called the Frenet–Serret equations.[49] If the curvature κ and the torsion τ of $\mathscr{C}$ are known for $0 \le s \le L$, the Frenet frame $\{\mathbf{t},\mathbf{n},\mathbf{b}\}$ can be obtained as the unique solution of the Frenet–Serret equations (1). In other words, the orthogonal triad $\{\mathbf{t},\mathbf{n},\mathbf{b}\}$ on $\mathscr{C}$ evolves in space according to the Frenet–Serret equations (1).

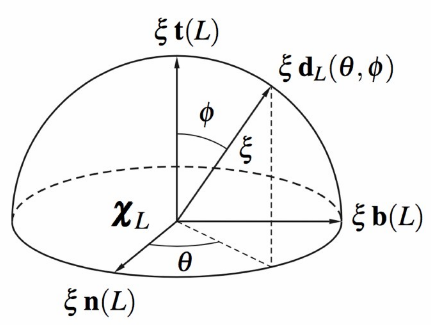

Fig. 2 An arbitrary molecule located on the end cap at $\boldsymbol{\chi}(L) = \boldsymbol{\chi}_L$, expressed as a linear combination of unit tangent $\mathbf{t}$, unit normal $\mathbf{n}$, and unit binormal $\mathbf{b}$ at the end point. The length of the molecule is denoted by ξ, and its orientation is represented by $\mathbf{d}_L(\theta,\phi)$.

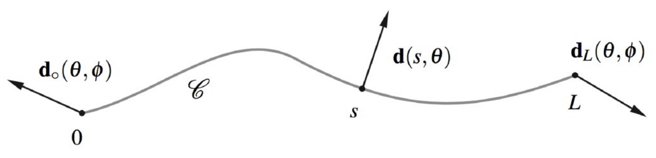

Fig. 1 Schematic of the centreline $\mathscr{C}$ of an open cylindrical micellar filament, and arbitrary molecules located on end caps and on the interior of $\mathscr{C}$. On the basis of our previous modeling assumptions,[21] the configuration of each amphiphile in the filament can be described by a point on $\mathscr{C}$ and a unit vector (i.e., a director), with the point representing the end of the rod and the director representing its orientation. Without loss of generality, the director tips are assumed to point toward the headgroups of the amphiphiles.

Let s belong to the open interval $(0,L)$, so that $\boldsymbol{\chi}(s)$ is interior to $\mathscr{C}$, and let θ denote the angle measured counterclockwise from $\mathbf{n}(s)$. Consider a molecule with tail at $\boldsymbol{\chi}(s)$. The head groups of the molecules at $\boldsymbol{\chi}(s)$ lie on the boundary of a disk (of radius ξ) in the plane spanned by $\mathbf{n}(s)$ and $\mathbf{b}(s)$. Relative to the Frenet frame, the director of a molecule with orientation θ at $\boldsymbol{\chi}(s)$ can therefore be expressed as $\mathbf{d}(s,\theta) = (\cos\theta)\mathbf{n}(s) + (\sin\theta)\mathbf{b}(s)$ (Figure 1). By Assumption i, the molecules at the endpoints $\boldsymbol{\chi}(0)$ and $\boldsymbol{\chi}(L)$ of $\mathscr{C}$ are arranged radially on hemispheres of radius ξ. Consider the endpoint $\boldsymbol{\chi}(L)$. Let ϕ denote the angle measured clockwise from $\mathbf{t}(L)$. Relative to the Frenet frame, the director $\mathbf{d}_L(\theta,\phi)$ of a molecule with orientation (θ,ϕ) at $\boldsymbol{\chi}(L)$ can thus be expressed as

$$\mathbf{d}_L(\theta,\phi) = \iota_n^L\,\mathbf{n}(L) + \iota_b^L\,\mathbf{b}(L) + \iota_t^L\,\mathbf{t}(L), \tag{2}$$

with $\iota_n^L = (\sin\phi)(\cos\theta)$, $\iota_b^L = (\sin\phi)(\sin\theta)$, and $\iota_t^L = \cos\phi$ (Figure 2). Similarly, the director $\mathbf{d}_\circ(\theta,\phi)$ of a molecule with orienta-

View Article Online
DOI: 10.1039/C7SM00911A

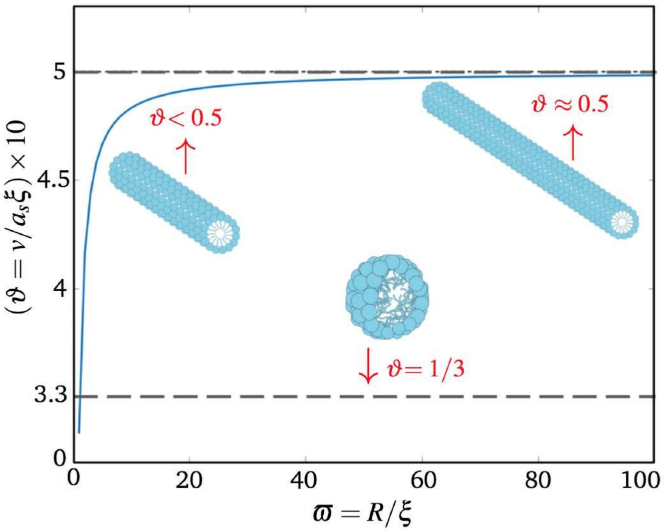

Fig. 3 Graph of the molecular packing parameter $v/a_s\xi$ against the ratio $\varpi = R/\xi$ based on our model. As observed in the plot, when ϖ increases, the packing parameter $\vartheta = v/a_s\xi$ approaches the value of CMC=1/2 for long cylindrical micellar filaments.

tion (θ,ϕ) at $\boldsymbol{\chi}(0)$ can be expressed as

$$\mathbf{d}_\circ(\theta,\phi) = \iota_n^\circ\,\mathbf{n}(0) + \iota_b^\circ\,\mathbf{b}(0) + \iota_t^\circ\,\mathbf{t}(0), \tag{3}$$

with $\iota_n^\circ = \iota_n^L$, $\iota_b^\circ = \iota_b^L$, and $\iota_t^\circ = -\iota_t^L$. It should be noted that ϕ in (3) is measured clockwise from $-\mathbf{t}(0)$.

2.3 Molecular distribution and packing

The distribution of the molecules at a generic point s in the open interval $(0,L)$ along $\mathscr{C}$ is denoted by the molecular density function $\mathscr{D} = \mathscr{D}(s,\theta)$. It follows from our previous assumptions that the integral $N_b = \int_0^L\int_0^{2\pi}\mathscr{D}(s)\,\mathrm{d}\theta\,\mathrm{d}s = 2\pi\int_0^L\mathscr{D}(s)\,\mathrm{d}s$, represents the total number N_b of amphiphiles comprising the cylindrical body of the micellar filament. According to item ii in section 2.1, end caps are assumed to have the same number of molecules. Let $\mathscr{D}_e(\theta,\phi)$ denote the molecular number density of the end caps at the endpoints $s=0$ and $s=L$. The number N_c of amphiphiles in either of the end caps is thus given by $N_c = \int_0^{\pi/2}\int_0^{2\pi}\mathscr{D}_e(\theta,\phi)\,\mathrm{d}\theta\,\mathrm{d}\phi$.

The volume V_t of a filament is the sum of the volume V_{cyl} of the cylindrical body and that of the end caps, as $V_t = V_{\text{cyl}} + 2V_{\text{cap}}$. On denoting the hydrocarbon core volume of an amphiphile by v, N_b and N_c are obtained as $N_b = V_{\text{cyl}}/v = \pi\xi^2 L/v$, and $2N_c = V_{\text{cap}}/v = 4\pi\xi^3/3v$. According to Israelachvili *et al.*,[2] the molecular packing parameter ϑ of an amphiphile is defined as the ratio $v/a_s\xi$ of the liquid hydrocarbon core volume v to its surface area a_s multiplied by the hydrocarbon length ξ, and can be derived for simple micellar topologies from geometric arguments. For an amphiphilic system with the local radii of curvature R_1 and R_2, the packing parameter $v/a_s\xi$ is obtained as[1,2]

$$\vartheta = 1 + \frac{2\xi^2 - 3\xi(R_1+R_2)}{6R_1R_2}. \tag{4}$$

For an open cylindrical micellar filament of length L with two end caps and no junctions, two conditions must be satisfied in order for $N = N_b + 2N_c$ amphiphiles to form such a geometry: $Na_s = 4\pi\xi^2 + 2\pi\xi L$, and $Nv = \pi\xi^2 L + 4\pi\xi^3/3$. Solving these equations for the ratio $v/a_s\xi$, while defining $\digamma := \xi/L \ll 1$ for long cylindrical micellar filaments, yields

$$\vartheta = \lim_{\digamma\to 0}\left(\frac{3+4\digamma}{6+12\digamma}\right) = \frac{1}{2}. \tag{5}$$

According to the derivation of the micro-mechanical model for a filament of diameter 2ξ,[21] R_1 in (4) is equal to ξ and thus, the packing parameter ϑ in (4) becomes $(3R-\xi)/6R$, where $R = 1/\kappa$ denotes the radius of curvature of the centreline of the filament. Thus, the molecular packing parameter ϑ for long cylindrical micellar filaments for which $\xi \ll R$, is obtained as $v/a_s\xi = \lim_{\varpi\to\infty}\left(\frac{3\varpi-1}{6\varpi}\right) = 1/2$, with $\varpi := R/\xi$. The plot of the packing parameter ϑ versus the ratio $\varpi = R/\xi$ has been shown in Figure 3. Similar to the previous studies, when ϖ increases, the packing parameter ϑ approaches the value of $1/2$ for long cylindrical micellar filaments. The value of ϑ for spherical micelles without void is $1/3$. For a short cylindrical micellar filament, ϑ is between $1/3$ and $1/2$.

2.4 Review of the derivation of the elastic bending energy density

The elastic bending energy of a cylindrical micellar filament includes two main parts: the elastic bending energy of the cylindrical body, and that of the end caps. Branched micelles include more than two end caps along with Y-junctions that contribute to the net elastic energy of the micelle.[15,50] To find the elastic bending energy density of the cylindrical body at a point $\boldsymbol{\chi}$, the interactions between all amphiphiles within a cutoff distance δ from the ones at $\boldsymbol{\chi}$ are taken into account (Figure 4). Amphiphiles are modelled as one-dimensional rigid rods, perpendicular to the centreline $\mathscr{C}$ of the filament (Figure 1). Our derivation relies on applying the Taylor series expansion with respect to a dimensionless parameter $\varepsilon := \delta/\ell \ll 1$, where ℓ represents the smallest radius of curvature that the centreline $\mathscr{C}$ is capable of exhibiting. The elastic energy of an open filament results from integrating this density over the centreline $\mathscr{C}$ and adding the elastic energy due to end caps.

Consider two molecules, with directors $\mathbf{d}$ and $\mathbf{d}'$, located respectively at positions $\boldsymbol{\chi}$ and $\boldsymbol{\chi}'$ interior to $\mathscr{C}$. Let the the intermolecular potential (encompassing steric, electrostatic, Van der Waals, and other relevant effects) between the molecules under consideration be denoted by $\Omega(\boldsymbol{\chi},\boldsymbol{\chi}',\mathbf{d}',\mathbf{d}')$. Following Keller and Merchant,[51] we assume that the intermolecular potential $\Omega(\boldsymbol{\chi},\boldsymbol{\chi}',\mathbf{d},\mathbf{d}')$ between two molecules separated by a distance

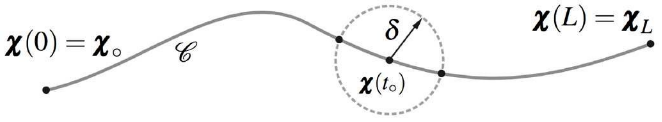

Fig. 4 Position $\boldsymbol{\chi}(t_\circ)$ and its vicinity, in which the interactions between the molecules located at $\boldsymbol{\chi}(t_\circ)$ and other molecules exist. The radius of the vicinity is the cutoff distance δ.

View Article Online
DOI: 10.1039/C7SM00911A

$|\boldsymbol{\chi}-\boldsymbol{\chi}'|$ more than a fixed cutoff distance δ vanishes. In the present setting, δ is required to be small relative to the minimum radius of curvature ℓ introduced in assumption iii,[21,47] so that $\delta \ll \ell$. Also, since the potential between a molecule at a given point on the micellar body and other molecules does not exist for the whole length of the micelle, the cutoff distance δ is assumed to be much smaller than the length L of the filament. Hereafter, we restrict attention to intermolecular potentials that are of the form $\Omega(\boldsymbol{\chi},\boldsymbol{\chi}',\mathbf{d},\mathbf{d}')$, but are also frame indifferent.[52] It then follows that $\Omega(\boldsymbol{\chi},\boldsymbol{\chi}',\mathbf{d},\mathbf{d}')$ may depend on the positions $\boldsymbol{\chi}$ and $\boldsymbol{\chi}'$ and the directors $\mathbf{d}$ and $\mathbf{d}'$ only through the length $|\boldsymbol{\chi}-\boldsymbol{\chi}'|$ of the vector between $\boldsymbol{\chi}$ and $\boldsymbol{\chi}'$, the dot products $(\boldsymbol{\chi}-\boldsymbol{\chi}')\cdot\mathbf{d}$ and $(\boldsymbol{\chi}-\boldsymbol{\chi}')\cdot\mathbf{d}'$ formed by the directors and that vector, and the dot product $\mathbf{d}\cdot\mathbf{d}'$ formed by the directors. Like Keller and Merchant,[51] we assume that the dependence of the intermolecular potential on the length of the relative position vector $\mathbf{r}=\boldsymbol{\chi}-\boldsymbol{\chi}'$ is scaled by the ratio ε. Therefore, we define $\tilde{\Omega}\big(\varepsilon^{-2}|\mathbf{r}|^2,\mathbf{r}\cdot\mathbf{d},\mathbf{r}\cdot\mathbf{d}',\mathbf{d}\cdot\mathbf{d}'\big)=\Omega(\boldsymbol{\chi},\boldsymbol{\chi}',\mathbf{d},\mathbf{d}')/2$ as the new form of the interaction potential (for more details, see Refs.[21,47]). The particular choice of the arguments of the intermolecular potential in its new form is in accord with those of the interaction potential between a pair of protein monomers forming a lipid bilayer, in which the pairwise intermolecular potential is a function of the relative position of the two protein particles and the orientation of each of the particles.[47,53] As a consequence of the foregoing discussion, the net free-energy ψ_b of the cylindrical body of the micelle can be expressed as

$$\psi_b=\int_0^L \frac{1}{2}\bigg(\int_0^{2\pi}\mathscr{E}(s,\theta)\,\mathrm{d}\theta\bigg)\mathscr{D}(s)\,\mathrm{d}s, \tag{6}$$

where the integrand of the inner integral, $\mathscr{E}(s,\theta)$, is

$$\mathscr{E}(s,\theta)=\int_0^L\!\!\int_0^{2\pi} 2\,\tilde{\Omega}(\mathscr{H}_1,\mathscr{H}_2,\mathscr{H}_3,\mathscr{H}_4)\mathscr{D}(t)\,\mathrm{d}\eta\,\mathrm{d}t, \tag{7}$$

with $\mathscr{H}_1=\varepsilon^{-2}|\boldsymbol{\chi}(s)-\boldsymbol{\chi}(t)|^2$, $\mathscr{H}_2=(\boldsymbol{\chi}(s)-\boldsymbol{\chi}(t))\cdot\mathbf{d}(s,\theta)$, $\mathscr{H}_3=(\boldsymbol{\chi}(s)-\boldsymbol{\chi}(t))\cdot\mathbf{d}(t,\eta)$, and $\mathscr{H}_4=\mathbf{d}(s,\theta)\cdot\mathbf{d}(t,\eta)$. Eq. (7) represents the total energy due to the interactions between the molecule with director $\mathbf{d}(s,\theta)$ at $\boldsymbol{\chi}(s)$ and all other molecules. A factor of one-half in (6) compensates for the double counting of interactions arising from integrating over both s and t from 0 to L. From (6), the elastic bending energy density $\psi(s)$ at position $\boldsymbol{\chi}(s)$ on $\mathscr{C}$ is simply

$$\psi(s)=\frac{1}{2}\bigg(\int_0^{2\pi}\mathscr{E}(s,\theta)\,\mathrm{d}\theta\bigg)\mathscr{D}(s). \tag{8}$$

Upon Taylor expanding the right-hand side of (8) up to two derivatives, the final form of the elastic bending energy density of the filament is found to be

$$\psi_{\text{mic}}=\psi_\circ+k_c\kappa^2+k_t\tau^2 \tag{9}$$

which is in terms of the curvature κ and torsion τ of the centreline $\mathscr{C}$. The configuration of the filament in the absence of stretch is uniquely determined, up to a rigid transformation, by the curvature κ and torsion τ of its centreline $\mathscr{C}$.[54] Notice that expression (9) is valid on the interior of $\mathscr{C}$ for $\delta<s<L-\delta$. In other words, the domain of interaction for molecules within the distance δ from an end cap includes the molecules at that end cap. This is not consistent with our underlying arguments. However, since $\delta \ll L$, it is reasonable to assume that (9) is valid within the whole domain $0<s<L$.

The sum of the quadratic terms on the right-hand side of the elastic bending energy density (9) resembles the corresponding bending free-energy functions for polymer chains,[38,39,55] FtsZ filaments,[56] and helical supramolecules such as DNA.[58,59] The term $\psi_\circ$ in the right-hand side of (9) represents a general inhomogeneous stretching energy density, which describes elongation. As shown in Eq. A.10 in Ref.,[21] this term depends upon the molecular distribution $\mathscr{D}$, as well as molecular dimensions. The bending rigidity $k_c=\frac{\partial^2\psi}{\partial\kappa^2}\Big|_{\kappa=0}$ in (9) quantifies the resistance of the micellar body against deviations from a uniform curvature, and takes positive values for stable aggregates to exist. Thus, mono-disperse objects with uniform rigid shapes are expected to possess large bending stiffness k_c, while poly-disperse flexible structures that are geometrically heterogeneous, are expected to have low values of this quantity. The torsional rigidity $k_t=\frac{\partial^2\psi}{\partial\tau^2}\Big|_{\tau=0}$ denotes the resistance of the micellar body against the torsion of $\mathscr{C}$ at each point. Both k_c and k_t, depend not only upon the size, composition, and distribution of amphiphiles along $\mathscr{C}$, but also on the temperature and the concentration of the solution.[57]

2.5 Elastic bending energy of an end cap

According to our micro-mechanical model,[21] the elastic bending energy of an end cap in an open micellar filament is determined by the interactions between the molecules located at the end cap and the ones located within the portion of the cylindrical body of the filament that lies within the cutoff distance δ. The schematic of the end point $\boldsymbol{\chi}_L$ of $\mathscr{C}$ is shown in Figure 5. By assumptions i and ii in section 2.1, each of the end caps is a hemisphere with radius equal to the length of an amphiphile (Figure 2). Following such assumptions, since the number of the molecules at the end caps and their distribution are considered to be the same, the geometries of the two end caps are identical. Therefore, the elastic bending energy of the two end caps is the same. In other words, the only reason we can distinguish the end caps is because we have oriented the filament. Thus, according to assumption iv, if we flip the orientation, the elastic bending energy does not change. Here, we derive an expression for the elastic bending energy of the end cap at $\boldsymbol{\chi}_L$.

The elastic bending energy $\bar{\psi}^{\text{cap}}$ of the end cap at $\boldsymbol{\chi}_L$ is given by

$$\bar{\psi}^{\text{cap}}=\int_0^{\frac{\pi}{2}}\!\!\int_0^{2\pi}\frac{1}{2}\mathscr{E}_c(\theta,\phi)\mathscr{D}_e\,\mathrm{d}\theta\,\mathrm{d}\phi, \tag{10}$$

where

$$\mathscr{E}_c(\theta,\phi)=\int_0^L\!\!\int_0^{2\pi}\tilde{\Omega}\Big(\bar{\mathscr{H}_1},\bar{\mathscr{H}_2},\bar{\mathscr{H}_3},\bar{\mathscr{H}_4}\Big)\mathscr{D}(t)\,\mathrm{d}\eta\,\mathrm{d}t, \tag{11}$$

in which $\bar{\mathscr{H}_1}=\varepsilon^{-2}|\boldsymbol{\chi}_L-\boldsymbol{\chi}(t)|^2$, $\bar{\mathscr{H}_2}=(\boldsymbol{\chi}_L-\boldsymbol{\chi}(t))\cdot\mathbf{d}(L,\theta)$, $\bar{\mathscr{H}_3}=(\boldsymbol{\chi}_L-\boldsymbol{\chi}(t))\cdot\mathbf{d}(t,\eta)$, and $\bar{\mathscr{H}_4}=\mathbf{d}(L,\theta)\cdot\mathbf{d}(t,\eta)$ with $\bar{\mathbf{r}}=\boldsymbol{\chi}_L-\boldsymbol{\chi}(t)$. Upon replacing $\mathscr{E}_c(\theta,\phi)$ from (11) to (10), and Taylor expanding the right-hand side of (10) up to two derivatives, the specific steps of which appear in Appendix 9.1, the final form of the elastic

View Article Online
DOI: 10.1039/C7SM00911A

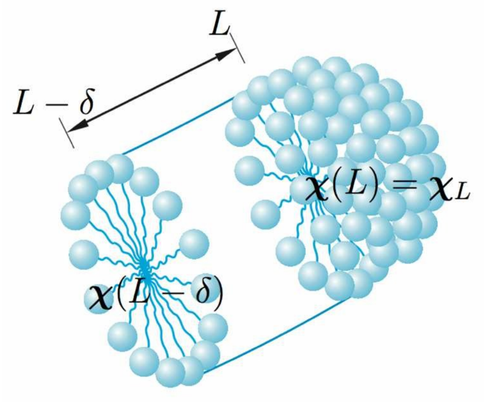

Fig. 5 Schematic of a hemispherical end cap attached to the cylindrical body, in which the caps have the same radius as the cylindrical body. The position $\boldsymbol{\chi}_L$ represents the centre of the hemisphere.

bending energy of the end cap at $\boldsymbol{\chi}_L$ is obtained as

$$\bar{\psi}^{\mathrm{cap}} = \bar{\psi}_{\circ}^{\mathrm{cap}} + \bar{k}_c^{\mathrm{cap}}\kappa_c^2 + \bar{k}_t^{\mathrm{cap}}\tau_c^2, \tag{12}$$

where κ_c and τ_c denote the curvature and torsion of $\mathscr{C}$ at the end point under consideration. The parameters $\bar{\psi}_{\circ}$, $\bar{k}_c$, and $\bar{k}_t$ are given as integral representations in terms of the molecular densities $\mathscr{D}_e$ and $\mathscr{D}$, and molecular dimensions in Appendix 9.1. Similar to the structure of (9), (12) is quadratic in the curvature and torsion at the endpoint under consideration.

A single open (unbranched) cylindrical micellar filament possesses two hemispherical end caps. The net elastic bending energy $\bar{\psi}^{\mathrm{cap}}$ of such a filament with centreline $\mathscr{C}$ is simply the sum of the elastic bending energy of the tubular body, and twice the elastic bending energy $\bar{\psi}^{\mathrm{cap}}$ corresponding to an end cap. Hence, $\mathscr{E}_{\mathrm{t}} = \int_{\mathscr{C}} \psi\, \mathrm{d}s + 2\,\bar{\psi}^{\mathrm{cap}}$, which, by (6)–(9) and (12), yields

$$\mathscr{E}_{\mathrm{t}} = \int_{\mathscr{C}} \psi\, \mathrm{d}s + 2\bar{\psi}_{\circ} + \bar{k}_c^{\mathrm{cap}}(\kappa_{\circ}^2 + \kappa_L^2) + \bar{k}_t^{\mathrm{cap}}(\tau_{\circ}^2 + \tau_L^2). \tag{13}$$

In (13), the subscripts $\circ$ and L are used to denote the values of the curvature κ and the torsion τ of $\mathscr{C}$ at endpoints $\boldsymbol{\chi}_0$ and $\boldsymbol{\chi}_L$. In dilute systems, surfactant exchange plays the most significant role in micellar growth. However, coalescence of short micelles is the primary cause of growth in highly concentrated micellar systems. In semi-dilute micellar systems, the end cap elastic bending energy is reported to be relatively high.[41,42] As a consequence, the elastic bending energy of a collection of cylindrical micellar filaments at equilibrium is minimized by reducing the number of end caps. Under certain conditions, this may be accompanied by elongation of micellar filaments.[42]

3 Continuum mechanical model

Continuum mechanics applies the principles of classical mechanics to a body regarded as a continuous medium. Using field equations such as the balance of mass, the balances of linear and angular momentum, and the balance of energy (i.e., the first law of thermodynamics), a set of coupled differential equations are obtained that govern the evolution of the body. The resulting theory is applicable to an arbitrary body that undergoes an arbitrary deformation. Our aim here is to find the continuum description of the elastic bending energy density of a cylindrical micellar filament. We assume that the length of the filament is much larger than its characteristic cross-sectional dimensions. Hence, we may employ the rod theory in our description of a micellar filament.

Cosserat medium (or directed continuum) denotes a material that possesses an internal microstructure, which affects its mechanical behaviour when considered as a continuous medium.[43,44,63] The Cosserat rod theory models the structure of a rod as a general curve furnished with two additional directors at each point. Such directors may denote the material lines in the cross-section. The material lines can stretch. They can also shear relative to each other as well as relative to the normal plane of the curve. In the context of *constrained* Cosserat rod theory, such directors might be considered as two orthogonal unit vectors lying within the cross-section, and perpendicular to the centreline.[43]

Here we apply constrained Cosserat rod theory to find the strain energy of a cylindrical micellar filament in the static state in the absence of extension of its centreline.

3.1 Kinematics of a constrained Cosserat rod

In the context of rod theory, the centreline $\mathscr{C}$ of a rod is indicated by a curve in the three-dimensional Euclidean space $\mathbb{R}^3$. A family of two-dimensional sets is also endowed to the centreline $\mathscr{C}$, to describe the material cross-section at each point. Hence, a rod with finite cross-sectional dimensions may be regarded as the mapping of the set $(s,\xi^1,\xi^2)\in\mathbb{R}^3$ (with $s\in[0,L]$, & $(\xi^1,\xi^2)\in a(s)$) into the three-dimensional Euclidean space $\mathbb{R}^3$, with $a(s)$ denoting the area of the cross-section of the rod at point s. Within the context of Cosserat rod theory,[43] the three-dimensional vector $\boldsymbol{\chi}(s)$ denotes the position of the centreline $\mathscr{C}$ of the rod relative to some fixed coordinate system. Further, each point on the centreline $\mathscr{C}$ corresponds to a value of s, and is endowed with a right-handed coordinate frame $\{\mathbf{d}_1,\mathbf{d}_2,\mathbf{d}_3\}$ of three linearly independent vectors (called directors). The director $\mathbf{d}_3$ is taken to be the tangent field $\mathbf{t}(s)=\dot{\boldsymbol{\chi}}(s)$. Notice that the directors $\mathbf{d}_1$ and $\mathbf{d}_2$ are not necessarily unit vectors, nor perpendicular to each other.[43] The position of a material point in the rod is then represented by[63,64]

$$\boldsymbol{\chi}^*(s,\xi^1,\xi^2) = \boldsymbol{\chi}(s) + \sum_{\alpha=1}^{2}\xi^{\alpha}\mathbf{d}_{\alpha}(s). \tag{14}$$

A Kirchhoff rod (i.e., a constrained Cosserat rod[43]), is identified by a collection of triples[64]

$$\{0<s<L|\,s\to\big(\boldsymbol{\chi}(s),\mathbf{d}_1(s),\mathbf{d}_2(s)\big)\in\mathbb{R}^3\}, \tag{15}$$

in which the directors $\mathbf{d}_1$ and $\mathbf{d}_2$ may be selected to be orthonormal, and also perpendicular to the unit tangent $\mathbf{t}$ so that $\mathbf{d}_1\cdot(\mathbf{d}_2\times\mathbf{t})=1$. In this case, the material cross-section at any point of the centreline $\mathscr{C}$ of the rod is assumed to lie within the plane orthogonal to the centreline at that point. Let the two perpendicular directors $\mathbf{d}_1$ and $\mathbf{d}_2$ denote the orientation of the two principal axes of inertia of the cross-section of the rod. Since the directors $\mathbf{d}_1$ and $\mathbf{d}_2$ lie within the plane spanned by the unit normal $\mathbf{n}$ and unit binormal $\mathbf{b}$ of the Frenet frame of the centreline

View Article Online
DOI: 10.1039/C7SM00911A

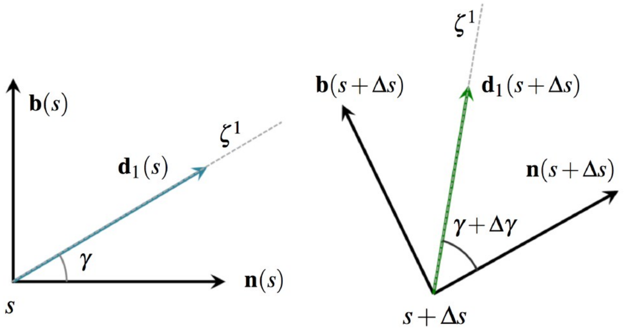

Fig. 6 Schematic of a material line element with the director $\mathbf{d}_1$ at the cross sections of the rod at s and $s+\Delta s$ with Δs being an infinitesimal increment of arc-length. The parameter γ represents the angle between the material line element and the unit normal $\mathbf{n}$ at the cross-section at s, and $\gamma+\Delta\gamma$ denotes the same quantity at the cross-section at $s+\Delta s$. The relative rotation of the material line element within the plane spanned by $\mathbf{b}$ and $\mathbf{n}$ is denoted by $\Delta\gamma$.

$\mathscr{C}$, they are related to $\mathbf{n}$ and $\mathbf{b}$ by a rotation about the unit tangent $\mathbf{t}$ through an angle $\gamma=\gamma(s)$, such that

$$\left.\begin{aligned}\mathbf{d}_1 &= (\cos\gamma)\,\mathbf{n}(s)+(\sin\gamma)\,\mathbf{b}(s),\\ \mathbf{d}_2 &= -(\sin\gamma)\,\mathbf{n}(s)+(\cos\gamma)\,\mathbf{b}(s)\end{aligned}\right\}. \tag{16}$$

Further, $\mathbf{d}_1\times\mathbf{d}_2=\mathbf{d}_3=\mathbf{t}$. Thus, $\{\mathbf{d}_1,\mathbf{d}_2,\mathbf{d}_3\}$ form a triad at each point. The evolution of directors along the centreline $\mathscr{C}$ is obtained by $\dot{\mathbf{d}}_i=\mathbf{u}\times\mathbf{d}_i$ for $i=\{1,2,3\}$, where $\mathbf{u}$ denotes the strain vector[64,65]

$$\mathbf{u}=\sum_{i=1}^{3}u_i\,\mathbf{d}_i=\frac{1}{2}\sum_{i=1}^{3}(\mathbf{d}_i\times\dot{\mathbf{d}}_i), \tag{17}$$

with components $u_i=\sum_{j=1}^{3}\sum_{k=1}^{3}\varepsilon_{ijk}\,\dot{\mathbf{d}}_j\cdot\mathbf{d}_k/2$, where ε_{ijk} denotes the usual permutation symbol ($\varepsilon_{123}=\varepsilon_{231}=\varepsilon_{312}=1$, $\varepsilon_{321}=\varepsilon_{132}=\varepsilon_{213}=-1$, and $\varepsilon_{ijk}=0$ if any two of i, j, k are equal). Thus,

$$\left.\begin{aligned}u_1 &= \frac{1}{2}(\dot{\mathbf{d}}_2\cdot\mathbf{d}_3-\dot{\mathbf{d}}_3\cdot\mathbf{d}_2),\\ u_2 &= \frac{1}{2}(\dot{\mathbf{d}}_3\cdot\mathbf{d}_1-\dot{\mathbf{d}}_1\cdot\mathbf{d}_3),\\ u_3 &= \frac{1}{2}(\dot{\mathbf{d}}_1\cdot\mathbf{d}_2-\dot{\mathbf{d}}_2\cdot\mathbf{d}_1)\end{aligned}\right\}. \tag{18}$$

Since $\{\mathbf{d}_1,\mathbf{d}_2,\mathbf{d}_3\}$ is selected to be an orthonormal basis, $\mathbf{d}_i\cdot\mathbf{d}_j=\delta_{ij}$ for $i,j=\{1,2,3\}$, where the Kronecker delta δ_{ij} is 1 for $i=j$, and 0 for $i\neq j$. Thus, $\dot{\mathbf{d}}_1\cdot\mathbf{d}_2=-\mathbf{d}_1\cdot\dot{\mathbf{d}}_2$, $\dot{\mathbf{d}}_1\cdot\mathbf{d}_3=-\mathbf{d}_1\cdot\dot{\mathbf{d}}_3$, and $\dot{\mathbf{d}}_2\cdot\mathbf{d}_3=-\mathbf{d}_2\cdot\dot{\mathbf{d}}_3$. Hence, the components u_i ($i=1,2,3$) of the twist vector $\mathbf{u}=u_i\,\mathbf{d}_i$ in (18) are obtained in terms of the curvature κ and twist $\tau+\dot{\gamma}$, with respect to the $\{\mathbf{d}_1,\mathbf{d}_2,\mathbf{d}_3\}$ triad, as

$$\mathbf{u}=(\kappa\sin\gamma)\,\mathbf{d}_1+(\kappa\cos\gamma)\,\mathbf{d}_2+(\tau+\dot{\gamma})\,\mathbf{d}_3. \tag{19}$$

Equivalently, using (16) in (19) gives the twist vector $\mathbf{u}$ with the following form in the Frenet basis

$$\mathbf{u}=\kappa\,\mathbf{b}+(\tau+\dot{\gamma})\,\mathbf{t}. \tag{20}$$

The curved shape of the centreline of a rod is completely determined by its two reference parameter fields (i.e., bending density or curvature κ, and torsion τ). The twist density in a rod is defined as the sum of the torsion τ of the centreline $\mathscr{C}$, and the term $\dot{\gamma}$, and is obtained by $\tau+\dot{\gamma}=\sum_{i=1}^{3}(\mathbf{d}_i\times\dot{\mathbf{d}}_i)\cdot\mathbf{t}$. Consider two material cross sections of the rod at points corresponding to s and $s+\Delta s$, with Δs being a small increment of arc-length. The parameter γ represents the angle between the material line element represented by the director $\mathbf{d}_1$ and the unit normal $\mathbf{n}$ at the cross-section at s, and $\gamma+\Delta\gamma$ denotes its counterpart at the cross-section at $s+\Delta s$, as depicted schematically in Figure 6. The quantity $\dot{\gamma}=\lim_{\Delta s\to 0}\Delta\gamma/\Delta s$ measures the rotation of the material line element with orientation $\mathbf{d}_1$ about the unit tangent $\mathbf{t}$ in the cross-section of the rod. The curvature κ and the twist density $\tau+\dot{\gamma}$ together with the Frenet frame $\{\mathbf{b},\mathbf{t},\mathbf{n}\}$ define the strain field $\mathbf{u}$ expressed in (20).

3.2 Linear and angular momentum balances

To reiterate, we consider the micellar filament to be made of a sequence of infinitesimal disks perpendicular to its centreline. Consider a traction vector $\mathbf{f}(s)$ corresponding the internal contact forces in the structure of a rod, and a couple force field $\mathbf{m}(s)$ corresponding the internal moment of the rod. In the absence of external force and external moment, the local forms of the linear and angular momentum balances for the rod in the static (i.e., time-independent) state are given by the two independent vectorial equations[63–66]

$$\dot{\mathbf{f}}+\boldsymbol{\gamma}=\mathbf{0}, \quad \text{and} \quad \dot{\mathbf{m}}+\dot{\boldsymbol{\chi}}\times\mathbf{f}+\boldsymbol{\beta}=0, \tag{21}$$

with $\dot{\boldsymbol{\chi}}(s)=\mathbf{t}(s)$, and $\boldsymbol{\gamma}(s)$ and $\boldsymbol{\beta}(s)$ representing, respectively, the external body force and external body couple per unit arc-length, applied on the cross section at $\boldsymbol{\chi}(s)$. Various effects such as gravity, electrostatics or self-contact interactions between different parts of the rod, or interaction with solvent, can be modeled by using different functional forms of the body force $\boldsymbol{\gamma}(s)$ and body couple $\boldsymbol{\beta}(s)$.

3.3 Constitutive model

Regardless of the body force and body couple, the number of unknowns in (21) exceeds the number of available equations. Hence, to close the system, additional information relating the kinetic quantities (i.e., local forces and moments) to the kinematic ones (i.e., curvature and torsion) are required. Following van der Heijden,[68] we consider linear constitutive relations between the components of the internal moment $\mathbf{m}=\sum_{i=1}^{3}m_i\,\mathbf{d}_i$, and those of the strain vector $\mathbf{u}=\sum_{i=1}^{3}u_i\,\mathbf{d}_i$ as $m_1=\mathbb{k}_1u_1$, $m_2=\mathbb{k}_2u_2$, and $m_3=\mathbb{k}_tu_3$, where $\mathbb{k}_1$ and $\mathbb{k}_2$ denote, respectively, the flexural rigidities of the rod about the principal axes of its cross-section whose orientations are represented by the directors $\mathbf{d}_1$ and $\mathbf{d}_2$. Further, $\mathbb{k}_3$ represents the twisting stiffness of the rod about $\mathbf{d}_3=\mathbf{t}$. According to the symmetry of the cross-section in our model, the flexural rigidities of the rod about the directors $\mathbf{d}_1$ and $\mathbf{d}_2$ are equal, and thus, $\mathbb{k}_1=\mathbb{k}_2=\mathbb{k}_c$. As a consequence, the internal moment $\mathbf{m}$ is expressed in terms of the curvature κ and twist $\tau+\dot{\gamma}$ of the centreline $\mathscr{C}$ in the $\{\mathbf{d}_1,\mathbf{d}_2,\mathbf{d}_3\}$ frame through

View Article Online
DOI: 10.1039/C7SM00911A

the particular form

$$\mathbf{m} = \mathbb{k}_c(\kappa \sin\gamma\,\mathbf{d}_1 + \kappa\cos\gamma\,\mathbf{d}_2) + \mathbb{k}_t(\tau + \dot{\gamma})\,\mathbf{d}_3, \tag{22}$$

or, equivalently, in the Frenet frame, as

$$\mathbf{m} = \mathbb{k}_c\kappa\,\mathbf{b} + \mathbb{k}_t(\tau+\dot{\gamma})\,\mathbf{t}. \tag{23}$$

The local equilibrium equations (21) together with the constitutive model (22) constitute three vectorial equations, which incorporate the local basis $\{\mathbf{d}_1, \mathbf{d}_2, \mathbf{d}_3\}$, the internal force $\mathbf{f}$, and the internal moment $\mathbf{m}$. Since $\mathbf{d}_1$, $\mathbf{d}_2$, and $\mathbf{d}_3$ are assumed to be orthonormal, and that $\mathbf{d}_3 = \dot{\boldsymbol{\chi}}$, only one of the directors $\{\mathbf{d}_1, \mathbf{d}_2\}$ needs to be found through (21) and (22). Hence, the system of three vectorial equations (21) and (22) is determined. The arc-length derivative of the internal moment $\mathbf{m}$ in (23) takes the form

$$\dot{\mathbf{m}} = \mathbb{k}_c\dot{\kappa}\,\mathbf{b} + \mathbb{k}_t\dot{\tau}\,\mathbf{t} + (\mathbb{k}_t - \mathbb{k}_c)\kappa\tau\,\mathbf{n}. \tag{24}$$

Using (24) in $(21)_2$ while ignoring the effects of the body force $\boldsymbol{\gamma}$ and body couple $\boldsymbol{\beta}$, yields

$$\mathbf{f}\times\mathbf{t} = \mathbb{k}_c\dot{\kappa}\,\mathbf{b} + \mathbb{k}_t\dot{\tau}\,\mathbf{t} + (\mathbb{k}_t - \mathbb{k}_c)\kappa\tau\,\mathbf{n}. \tag{25}$$

Performing cross-product of both sides of (25) by the unit tangent $\mathbf{t}$, and using the vectorial identity $\mathbf{u}\times(\mathbf{v}\times\mathbf{w}) = (\mathbf{u}\cdot\mathbf{w})\mathbf{v} - (\mathbf{w}\cdot\mathbf{v})\mathbf{v}$, we obtain

$$\mathbf{f} = f_t\,\mathbf{t} - \mathbb{k}_c\dot{\kappa}\,\mathbf{n} + (\mathbb{k}_t - \mathbb{k}_c)\kappa\tau\,\mathbf{b}, \tag{26}$$

where $f_t = \mathbf{f}\cdot\mathbf{t}$. The strain energy $\mathscr{F}$ of the rod is then obtained by[71]

$$\mathscr{F} = \frac{1}{2}\int_0^L \mathbf{m}\cdot\mathbf{u}\,\mathrm{d}s = \int_{\mathscr{C}} \psi_{\mathrm{con}}. \tag{27}$$

In view of (20) and (23), the strain-energy density ψ_{con} in (27), which is quadratic in the components of the twist vector $\mathbf{u}$, is obtained with the particular form

$$\psi_{\mathrm{con}} = \frac{1}{2}\mathbf{m}\cdot\mathbf{u} = \frac{1}{2}\mathbb{k}_c\,\kappa^2 + \frac{1}{2}\mathbb{k}_t(\tau+\dot{\gamma})^2. \tag{28}$$

According to the elementary mechanics of materials,[69] if we assume a linear isotropic elastic constitutive model for the rod, the flexural rigidities $\mathbb{k}_1$ and $\mathbb{k}_2$, and the twisting stiffness $\mathbb{k}_t$ can be expressed in terms of the principal second moments of inertia I_1 and I_2 about the directors $\mathbf{d}_1$ and $\mathbf{d}_2$ (which denote the principal axes of the cross-section of the rod), the polar moment of inertia J, the elastic modulus E, and the shear modulus G, as $\mathbb{k}_1 = EI_1$, $\mathbb{k}_2 = EI_2$, and $\mathbb{k}_3 = JG$. Alternatively, for a cylindrical rod of radius ξ, we can say $I_1 = I_2 = \pi\xi^4/4$, and $J = 2I_1$. Thus, $\mathbb{k}_c$ and $\mathbb{k}_t$ can be expressed as $\mathbb{k}_c = EI = \pi E\xi^4/4$ and $\mathbb{k}_t = GJ = \pi G\xi^4/2$, respectively. Hence, the resulting strain-energy density ψ_{con} in (28) takes the form of the commonly used function for linear isotropic elastic cylindrical rods with no axial extension,[65] as

$$\psi_{\mathrm{con}} = \frac{1}{2}EI\,\kappa^2 + \frac{1}{2}JG(\tau+\dot{\gamma})^2 = \frac{\pi\xi^4 E}{8}\,\kappa^2 + \frac{\pi\xi^4 G}{4}(\tau+\dot{\gamma})^2. \tag{29}$$

In view of $G = E/2(1+\nu)$, (29) simplifies to

$$\psi_{\mathrm{con}} = \frac{\pi\xi^4 E}{8(1+\nu)}\Big((1+\nu)\kappa^2 + (\tau+\dot{\gamma})^2\Big). \tag{30}$$

The elastic bending energy density ψ_{con} in (30) contains two material parameters: the elastic modulus E and the Poisson's ratio ν. These two material parameters can be measured through relevant experiments. The majority of the previous studies on biofilaments take Poisson's ratio ν as 0.5 by assuming incompressibility of the filament.

4 Comparative merits of the two models

The continuum description of the elastic bending energy density of micellar filaments is found to resemble the previously derived micro-mechanical perspective. However, the terms corresponding to torsion and twist are found to be different. The micro-mechanical model considers the cross-section of the micelle as a set of amphiphiles with a uniform angular distribution. The amphiphiles are assumed to be free to rotate relative to each other, and thus, their rotation within the cross-section (i.e., the plane spanned by the unit normal $\mathbf{n}$ and binormal $\mathbf{b}$) does not expend energy. Consequently, within the micro-mechanical setting, the term $\dot{\gamma}$ does not appear in the resulting elastic bending energy density function (9). However, in the continuum model, the cross-section of the micellar filament is observed as a continuous area whose material lines are not free to rotate relative to each other. Hence, within the continuum mechanical setting, any relative rotation between the material fibers within the cross-section has an energy cost. Thus, the relative rotation $\dot{\gamma}$ does appear in the continuum model. In other words, the continuum mechanical model includes the relative rotation of the material line elements within the cross-section through the term $\dot{\gamma}$. Intuitively, the rotation of a generic point on the cross-section of the filament is the sum of the rotation of the centreline (represented by the torsion τ), and the rotation of the cross-section relative to the centreline (i.e., the twist angle of the cross-section about the centreline, denoted by the term $\dot{\gamma}$). Consequently, the torsional rigidity k_t in the micro-mechanical model (9) is not the same as the macroscopic twisting rigidity $\mathbb{k}_t$ in the continuum model (28).

Contrary to the continuum mechanical model that does not yield specific expressions for the flexural and twisting rigidities of the micellar filament, the derivation of the micro-mechanical model establishes unique relationships between those material parameters of the micellar filament at any point, and the microscopic features such as molecular size, molecular distribution, and molecular interactions. Such relationships appear in the form of integral representations for the elastic moduli of the micellar filament in terms of a generic interaction potential. To compute the flexural and torsional rigidities $\bar{k}_c$ and $\bar{k}_t$ at the end caps, we apply an anisotropic Gaussian potential, which describes the interaction between axisymmetric rod-like molecules.[60,61] However, a simplifying assumption must be imposed: that the molecules comprising the filament are identical and uniformly distributed. The resulting moduli are described in terms of several parameters. Aside from the molecular distribution function, these parameters fall into two separate categories: those appearing in the structure of the interaction potential, and those determined by molecular dimensions. The interaction between two rod-like molecules with

View Article Online
DOI: 10.1039/C7SM00911A

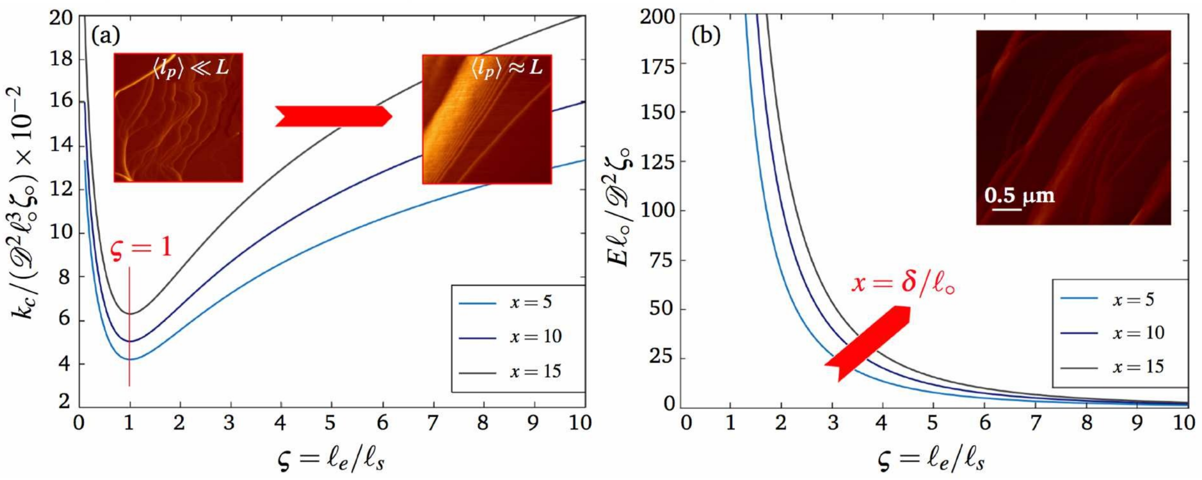

Fig. 7 (a) Plot of the dimensionless flexural rigidity $k_c/(\mathscr{D}^2\sigma_\circ^3\zeta_\circ)$ against the molecular aspect ratio $\varsigma = \ell_e/\ell_s$ as a consequence of applying modified Berne–Pechukas interaction potential for selected values of the dimensionless cutoff distance $x = \delta/\ell_\circ$; (b) Plot of the dimensionless elastic modulus $E\ell_\circ/\mathscr{D}^2\zeta_\circ$ against the molecular aspect ratio $\varsigma = \ell_e/\ell_s$ for different choices of $x = \delta/\ell_\circ$. The flexural rigidity k_c is a mechanical characteristic, which combines a geometric feature (i.e., the second moment of inertia I) and a material property (i.e., the elastic modulus E).

the orientations $\mathbf{d}$ and $\mathbf{e}$ in such a potential, is given by

$$\hat{\Omega}(\mathbf{r},\mathbf{d},\mathbf{e}) = \prod_{i=1}^{3}\hat{\zeta}_i(\mathbf{r};\mathbf{d},\mathbf{e}), \tag{31}$$

where $\hat{\zeta}_1(\mathbf{d},\mathbf{e})\,\hat{\zeta}_2(\hat{\mathbf{r}},\mathbf{d},\mathbf{e})$ denotes the strength parameter, with $\hat{\zeta}_1(\mathbf{d},\mathbf{e})$ and $\hat{\zeta}_2(\hat{\mathbf{r}},\mathbf{d},\mathbf{e})$ respectively expressed as

$$\left(\frac{4\,\zeta_\circ}{\sqrt{1-\chi^2(\mathbf{d}\cdot\mathbf{e})^2}}\right)^{\mu_1}, \tag{32}$$

and

$$\left(1-\frac{\chi'}{2}\left(\frac{(\hat{\mathbf{r}}\cdot\mathbf{d}+\hat{\mathbf{r}}\cdot\mathbf{e})^2}{1+\chi'\mathbf{d}\cdot\mathbf{e}}+\frac{(\hat{\mathbf{r}}\cdot\mathbf{d}-\hat{\mathbf{r}}\cdot\mathbf{e})^2}{1-\chi'\mathbf{d}\cdot\mathbf{e}}\right)\right)^{\mu_2}. \tag{33}$$

Further, $\hat{\zeta}_3(\hat{\mathbf{r}},\mathbf{d},\mathbf{e})$ represents the distance parameter with the form $\hat{\zeta}_3(\hat{\mathbf{r}},\mathbf{d},\mathbf{e}) = \exp(-|\mathbf{r}|^2/\hat{\sigma}^2(\mathbf{r},\mathbf{d},\mathbf{e}))$.[61] In (32), $\zeta_\circ$ is a fitting parameter, μ_1 and μ_2 denote parameters specifying the type of amphiphiles, and $\hat{\mathbf{r}}$ represents the unit vector corresponding to the intermolecular vector $\mathbf{r}$. The parameter χ in (32) is related to the anisotropy in the shape of the molecule, and is given in terms of the ratio $\varsigma = \ell_e/\ell_s$ of the length ℓ_e of the molecule to its breadth ℓ_s by $\chi = (\varsigma^2-1)/(\varsigma^2+1)$. Also, χ' in (33) is given by $\chi' = (\bar{\varepsilon}^{1/\mu_2}-1)/(\bar{\varepsilon}^{1/\mu_2}+1)$, where $\bar{\varepsilon} = \varepsilon_e/\varepsilon_s$ denotes the ratio of the strength parameter for end-to-end and side-to-side configurations. Also, $\hat{\sigma}(\hat{\mathbf{r}},\mathbf{d},\mathbf{e})$ is called the range parameter and is given by $\hat{\sigma}/2\ell_s = 1/\left(2-\chi\left(\frac{(\hat{\mathbf{r}}\cdot\mathbf{d}+\hat{\mathbf{r}}\cdot\mathbf{e})^2}{1+\chi\mathbf{d}\cdot\mathbf{e}}+\frac{(\hat{\mathbf{r}}\cdot\mathbf{d}-\hat{\mathbf{r}}\cdot\mathbf{e})^2}{1-\chi\mathbf{d}\cdot\mathbf{e}}\right)\right)^{1/2}$. The parameters μ_1 and μ_2 are selected to be -1 and 2 respectively.[62] The flexural rigidity k_c was previously obtained in terms of the constant molecular distribution function $\mathscr{D}$, the fitting parameter $\zeta_\circ$, the length scale $\ell_\circ$, and the dimensionless parameter $x = \delta/\ell_\circ$ (Eq. 41 in Ref.[21]). The bending rigidity k_c of a rod with a circular cross-section of radius ℓ_e is $EI = \pi E\ell_e^4/4$. This, together with $\ell_\circ = \sqrt{2}\ell_s$, gives the local elastic modulus of the filament as

$$\frac{E}{4\mathscr{D}^2\zeta_\circ k_BT} = \frac{2.7\,\mathrm{erf}(x)\left(\chi^2\mathscr{L}+\mathscr{I}\right)+\chi^2 xe^{-x^2}\left(2x^2-3\right)\mathscr{L}}{3\pi\varsigma^4\ell_\circ k_BT}, \tag{34}$$

where "erf" represents the error function and $\mathscr{L}$ is the sum of $\mathscr{I}$ and $\mathscr{J}$, two integral representations in Eq.(43) in Ref.[21] Here we use the dimensions of a specific amphiphile (CTASal/NaSal/Water).[48] The length of this particular amphiphile from head-group to tail is about 2 nm, and the diameters of the head-group and tail are 0.85 nm and 0.5 nm, respectively. Setting the length and volume of the amphiphile equal to those of the replacing spheroid, the aspect ratio ℓ_e/ℓ_s is found to be ≈ 5.[21] Figures 7_a & 7_b display the dimensionless flexural rigidity $k_c/(\mathscr{D}^2\sigma_\circ^3\zeta_\circ)$ and the dimensionless elastic modulus $E\ell_\circ/\mathscr{D}^2\zeta_\circ$ of the cylindrical body of the filament against the molecular aspect ratio $\varsigma = \ell_e/\ell_s$, for selected values of the dimensionless cutoff distance $x = \delta/\ell_\circ$. A consequence of (34) is that the elastic modulus E increases as the dimensionless cutoff distance $x = \delta/\ell_\circ$ increases for fixed values of the molecular aspect ratio $\varsigma = \ell_e/\ell_s$. Thus, the model predicts a monotonic increase in the local flexural rigidity of the filament when increasing the molecular aspect ratio (see Figure 7_a). Also, as Figure 7_b depicts, the elastic modulus E diminishes as the molecular aspect ratio $\varsigma = \ell_e/\ell_s$ increases for fixed values of $x = \delta/\ell_\circ$. (Molecular dimensions determine the diameter of the filament.) This finding is consistent with the results of Jennings *et al.*,[67] who reported that the elastic modulus of the micelles depends upon micellar diameter. According to their findings,[67] an increase in the diameter of the micellar filament is accompanied by a decrease in the elastic modulus of the filament. The decrease in the elastic modulus E is compensated by the increase in the second moment of inertia $I = \pi\xi^4/4$, as the molecular aspect ratio, or equivalently, the diameter 2ξ of the filament increases. The consequence is an increase in the local flexural rigidity EI as a result of an increase in the micellar diameter.

By applying the interaction potential (31) on (12) using (40), the dimensionless form $\bar{\psi}_\circ^{\mathrm{cap}}/(\mathscr{D}\mathscr{D}_e\ell_\circ\zeta_\circ)$ of the homogeneous term

View Article Online
DOI: 10.1039/C7SM00911A

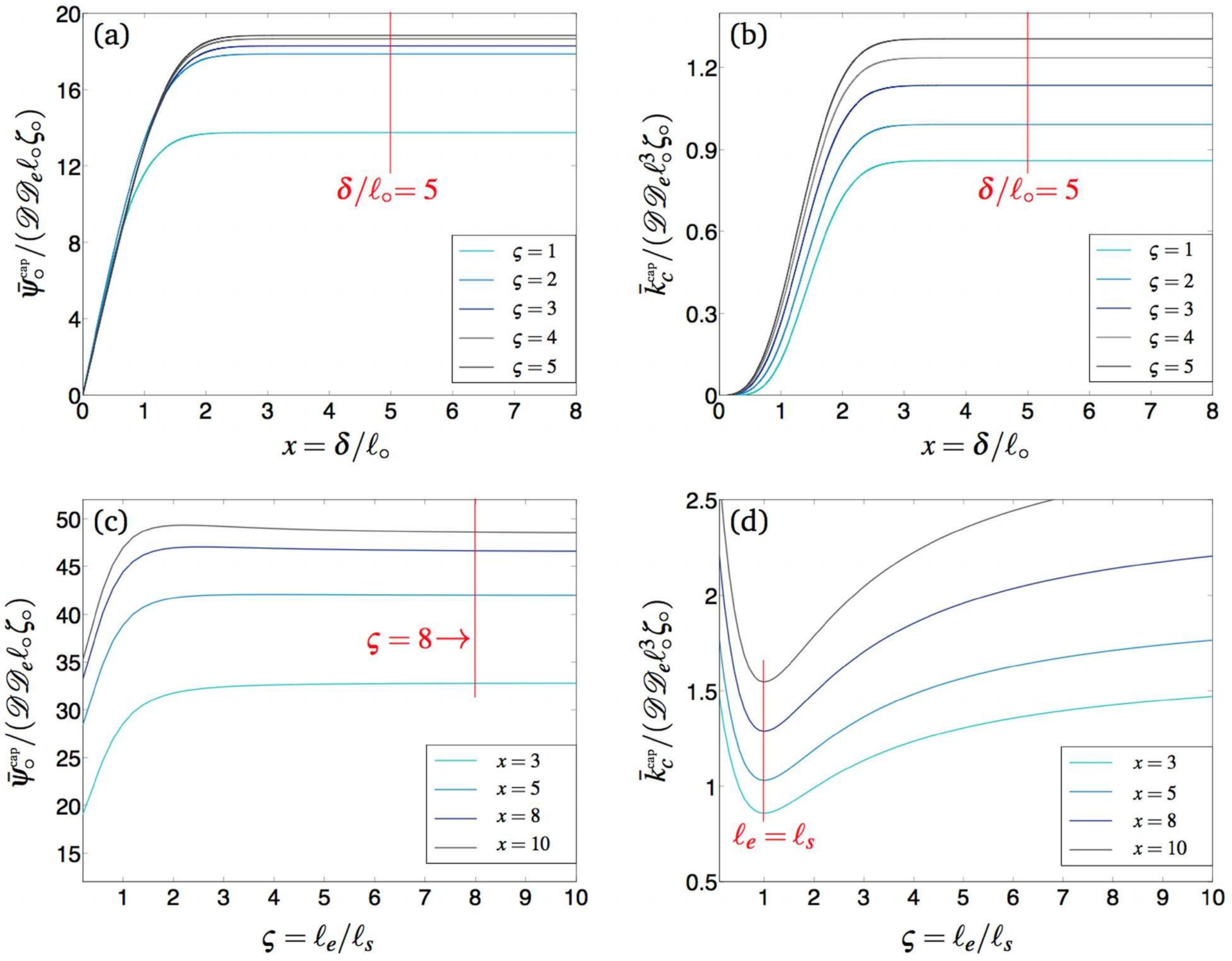

Fig. 8 (a) & (b): Plots of the dimensionless parameter $\bar{\psi}_\circ^{\rm cap}/(\mathscr{D}\mathscr{D}_e\ell_\circ\zeta_\circ)$, and the dimensionless flexural rigidity $\bar{k}_c^{\rm cap}/(\mathscr{D}\mathscr{D}_e\ell_\circ^3\zeta_\circ)$ against the ratio $\delta/\ell_\circ$ as a result of applying modified Berne–Pechukas interaction potential for different choices of the aspect ratio $\varsigma=\ell_e/\ell_s$. As is evident from the plots, negligible change in $\bar{\psi}_\circ^{\rm cap}/(\mathscr{D}\mathscr{D}_e\ell_\circ\zeta_\circ)$ and $\bar{k}_c^{\rm cap}/(\mathscr{D}\mathscr{D}_e\ell_\circ^3\zeta_\circ)$ is observed for $\delta/\ell_\circ>5$. Hence, an effective cutoff distance after which the potential decays rapidly can be reasonably approximated by $\delta=5\ell_\circ$; (c) & (d): Plots of $\bar{\psi}_\circ^{\rm cap}/(\mathscr{D}\mathscr{D}_e\ell_\circ\zeta_\circ)$ and $\bar{k}_c^{\rm cap}/(\mathscr{D}\mathscr{D}_e\ell_\circ^3\zeta_\circ)$ in terms of the molecular aspect ratio $\varsigma=\ell_e/\ell_s$ for different values of the dimensionless cutoff distance $x=\delta/\ell_\circ$.

$\bar{\psi}_\circ^{\rm cap}$ at the end cap is obtained as

$$\frac{\bar{\psi}_\circ^{\rm cap}}{k_BT}=\frac{\mathscr{D}\mathscr{D}_e\ell_\circ\zeta_\circ}{16k_BT}\Big\{\chi(\mathscr{J}_1+\mathscr{J}_2)\Big(\sqrt{\pi}\,\mathrm{erf}(x)-2xe^{-x^2}\Big)+2\sqrt{\pi}\,\mathrm{erf}(x)\Big(2\chi'(\mathscr{J}_4-\mathscr{J}_3)+\mathscr{J}_5\Big)\Big\}. \quad (35)$$

Also, the end cap bending rigidity $\bar{k}_c^{\rm cap}/(\mathscr{D}\mathscr{D}_e\ell_\circ^3\zeta_\circ)$ is obtained as

$$\frac{\bar{k}_c}{k_BT}=\frac{\mathscr{D}\mathscr{D}_e\ell_\circ^3\zeta_\circ}{384k_BT}\Big\{3\sqrt{\pi}\,\mathrm{erf}(x)\Big(\mathscr{I}_1-\chi^2\mathscr{I}_2+4\chi^2\mathscr{I}_3\Big)+2xe^{-x^2}\Big((2x^2+3)(\chi^2\mathscr{I}_2-\mathscr{I}_1)-12\chi^2\mathscr{I}_3\Big)\Big\}, \quad (36)$$

where $\mathscr{I}_1$–$\mathscr{I}_3$ and $\mathscr{J}_1$–$\mathscr{J}_5$ are integral representations shown in Appendices 9.2 & 9.3. These two material parameters are plotted against the parameter $x=\delta/\ell_\circ$ for different choices of the molecular aspect ratios ℓ_e/ℓ_s between 1 and 5 (Figure 8). Figures 8_a, 8_b, 8_c, & 8_d show, respectively, the dimensionless forms of the parameter $\bar{\psi}_\circ^{\rm cap}/(\mathscr{D}\mathscr{D}_e\ell_\circ\zeta_\circ)$ and the flexural rigidity $\bar{k}_c^{\rm cap}/(\mathscr{D}\mathscr{D}_e\ell_\circ^3\zeta_\circ)$ at the end points against the ratio $x=\delta/\ell_\circ$ for different values of the aspect ratio $\varsigma=\ell_e/\ell_s$, and those dimensionless parameters versus the aspect ratio $\varsigma=\ell_e/\ell_s$, for different values of the ratio $x=\delta/\ell_\circ$. As Figures 8_a & 8_b display, negligible changes in $\bar{\psi}_\circ^{\rm cap}/(\mathscr{D}\mathscr{D}_e\ell_\circ\zeta_\circ)$ and $\bar{k}_c^{\rm cap}/(\mathscr{D}\mathscr{D}_e\ell_\circ^3\zeta_\circ)$ are observed for $\delta/\ell_\circ>5$. Hence, an effective cutoff distance for the end caps after which the potential decays rapidly, can be reasonably approximated by $\delta=5\ell_\circ$. As Figure 8_c displays, the dimensionless form of the homogeneous contribution $\bar{\psi}_\circ^{\rm cap}/(\mathscr{D}\mathscr{D}_e\ell_\circ\zeta_\circ)$ remains insensitive to an increase in the molecular aspect ratio $\zeta=\ell_e/\ell_s$ for fixed values of $x=\delta/\ell_\circ$. As an approximation, when $\zeta>8$, $\bar{\psi}_\circ^{\rm cap}$ reaches a horizontal asymptote. This homogeneous contribution to the end cap elastic bending energy is thus considered to be insensitive to the shape of the end cap, but may have implicit dependence upon effects such as temperature and solution concentration. The local flexural rigidity $\bar{k}_c^{\rm cap}$ at the end cap, however,

View Article Online
DOI: 10.1039/C7SM00911A

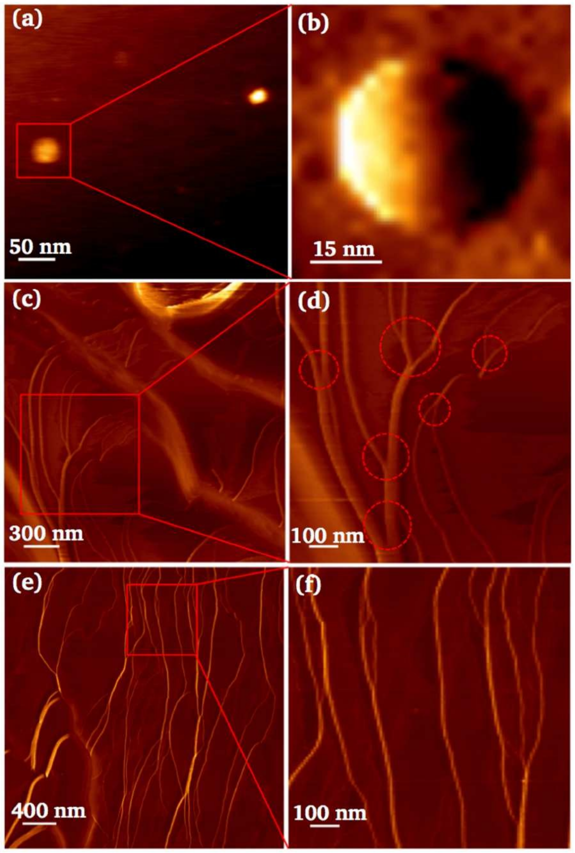

Fig. 9 Representative atomic force microscopy (AFM) contact mode images of spherical and cylindrical micelles; (a) & (b) Height images of spherical micelles in a dehydrated sample of dilute micellar system; (c) & (d) Vertical deflection images of a network of disseminated branched micelles with Y-junctions in a semidilute system in the dehydrated state and room temperature, formed through inter-micellar interactions;[29] (e) & (f) VD images of disseminated cylindrical micellar filaments as separated strands in hydrated state at room temperature. In semidilute and dense systems, the population of linear micelles increases and dominates when surfactant density increases.[21]

shows sensitivity to the molecular aspect ratio $\zeta = \ell_e/\ell_s$ at any fixed dimensionless cutoff distance $x = \delta/\ell_\circ$, which is consistent with the previous observations (Figure 8_d). Figures 8_a and 8_b show that as $\delta/\ell_\circ$ increases, $\bar{\psi}_\circ^{\text{cap}}$ and $\bar{k}_c^{\text{cap}}$ approach asymptotes. As is evident from the results of Figure 8, when the aspect ratio of the molecules increases, the flexural rigidity $\bar{k}_c^{\text{cap}}$ increases. When the aspect ratio of the molecules increases, a larger number of amphiphiles may aggregate at an end point. Hence, the filament is expected to be stiffer at those locations.

Each of the developed models for micellar filaments includes a number of material parameters that need to be found using different experiments. Some researchers fit the histogram of the experimental data (obtained from the size of the micellar chains) to a Gaussian function (i.e., the total volume fraction density, expressed in terms of the net elastic bending energy) to find the flexural rigidity of the filaments. Another experimental technique to measure the flexural rigidity of micellar filaments is small-angle neutron scattering (SANS).[77] Other studies suggest experiments such as the three-point bending test to find the elastic modulus E and the resulting flexural rigidity k_c of micellar filaments. Here we apply the nano-indentation test to measure the elastic modulus E of the tubular body of such filaments and that of the end caps. The indentation depth is related to the applied indentation force F and the stiffness of the AFM cantilever and that of the micellar filament. According to the Hertzian model, the elastic modulus E of the filament is expressed in terms of the applied load F by $E = 3F(1-\nu^2)/4\Delta\sqrt{R\Delta}$, where ν denotes Poisson's ratio of the filament (selected to be 0.5), Δ is the indentation depth, and R represents the effective radius, given as $R = R_1R_2/(R_1+R_2)$, in terms of R_1 and R_2, the radii of the applied AFM probe and the micellar filament.

5 Experimental section

Here we apply Atomic Force Microscopy (AFM) to measure the elastic modulus E of the micellar filaments through the indentation test using force volume analysis.

5.1 Materials and sample preparation

The dilute and semi-dilute micellar solutions included Hexadecyitrimethylammonium bromide (CTAB 50 mM, Sigma-Aldrich Corporation, ON, Canada) and the organic salt Sodium salicylate (NaSal 16 mM, Sigma-Aldrich Corporation, ON, Canada) with molar ratios NaSal/CTAB = 0.05 and 0.3 respectively, dissolved in sterile deionized water (ddH$_2$O) at room temperature.[70] Deionized water was added drop-wise using a calibrated pipette with 100 µL increments. To prepare the samples for AFM, 50 µL of the solution was deposited on a microscope slide for imaging and force spectroscopy. After 30 minutes, the sample was gently washed with deionized water. The sample was then set to dry in air at room temperature. Micellar filaments adhered strongly to the slide.

5.2 Atomic Force Microscopy

Atomic force microscopy (AFM) is a useful tool for exploring properties of materials at the micro and nano scales. It is able to quantify phenomena such as van der Waals interactions, electrostatic forces, and molecular bonds. It has extensive applications in fields such as polymers, DNA analysis, proteins, and biomaterials.[45,46] Using this powerful tool, various aspects of materials such as their topographical information, electrical conductivity, and mechanical stiffness can be investigated. Another feature of AFM is its ability to produce high-resolution images of materials. A sharp tip mounted on an AFM cantilever scans the surface of the sample, providing access to its topography at the nano scale. As the tip approaches the surface, the cantilever deflects due to the interactions between the tip and the surface. As the tip scans over the sample, a laser beam is focused on the back of the cantilever, whose deflection is measured by a detector. The measured deflections are reconstructed to create an image of the topography of the surface of the sample.

We used a JPK Atomic Force Microscope (JPK Nano-wizard@3 Bio-Science, Berlin, Germany) for imaging and force spectroscopy of micellar filaments. A biotool high resolution qp-BioAC/Quartz cantilever with a 2 nm defined conical tip, a spring constant of

View Article Online
DOI: 10.1039/C7SM00911A

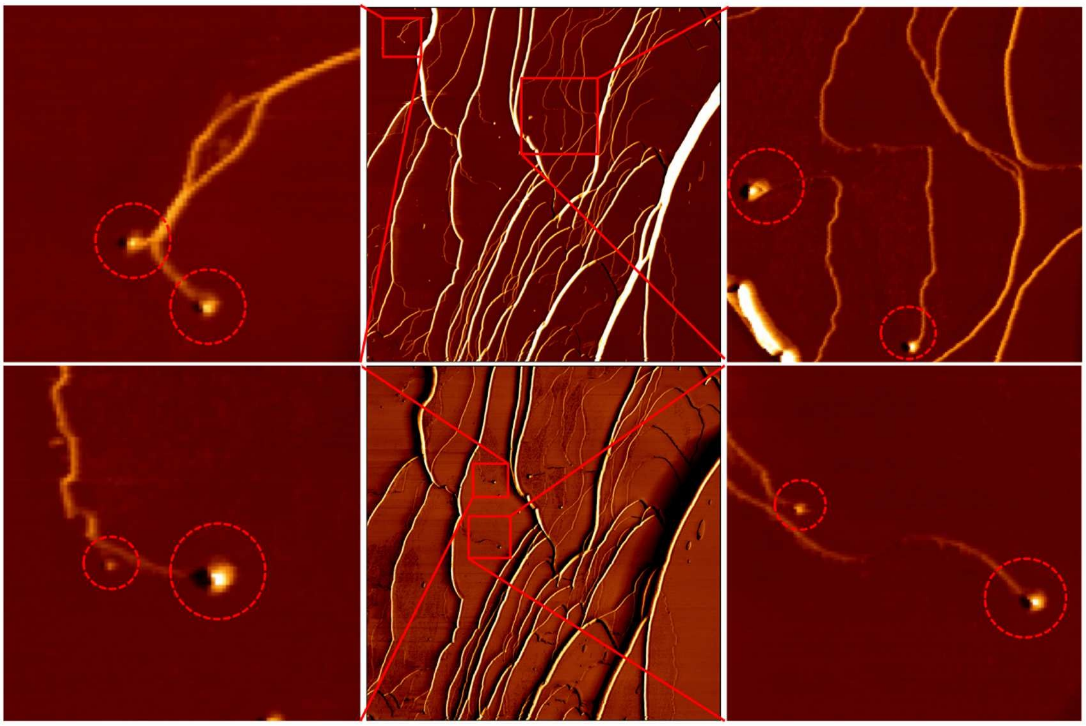

Fig. 10 AFM contact mode vertical and lateral deflection images of networks of disseminated open cylindrical micellar filaments with spherical end caps in the dehydrated state in a semi-dilute system at room temperature. For micellar filaments made of amphiphiles with a cylindrical packing characteristic, it has been reported that the final shape of the end caps is revealed once the micellar length is significantly greater than its cross-sectional dimensions.[42] As reported by May and Ben-Shaul[42] and observed here, the dimensions of end caps in shorter cylindrical micellar filaments are larger than those of their cylindrical body. However, when the end caps are molded into their final shape, they have the same radius as the cylindrical body.[42]

0.1 N/m, a nominal resonance frequency of 50 kHz in air, and a length of 60 μm (Nanotools USA LLC, Henderson, NV) was used for high resolution imaging of spherical micelles with radii from 10 to 75 nm[46] (Figures 9_a & 9_b), and micellar filaments with or without Y-junctions (Figures 9_c–9_f), or end caps (Figure 10). We used a Nanotools CONTR B50 cantilever with a spherical tip of 50 nm ± 10% and a spring constant of 0.2 N/m, a nominal resonance frequency of 13 kHz, and a length of 450 μm (Nanotools USA LLC, Henderson, NV) for indentation. Targeted filaments, which did not overlap, were located and indented. The indentation frequency was selected between 1 and 200 Hz. The deflection sensitivity of the piezo module was established by probing the surface of the mica substrate. A thermal tuning method was used to calibrate the stiffness of the cantilever. A force map containing 128×128 indentation points was created for each sample. The majority of the indented points within the created force map were analyzed using $\nu = 0.5$ and R_1=50 nm. The approaching force-indentation depth curve was applied to estimate the elastic modulus of the filaments.[45] AFM data analysis was carried out using the native JPK data processing software. Statistical significance was investigated using a paired student's t-test, and the differences were considered significant at $p<0.05$.

6 Results and discussion

Although some studies consider flexural rigidity as a material parameter,[36] our model accounts for flexural rigidity as the product of the second moment of inertia I of the micellar cross-section (i.e., a geometrical feature), and the elastic modulus E of the micelle (i.e., a material parameter). Thus, this mechanical characteristic depends upon the micellar diameter 2ξ, and its elastic modulus E, as shown in Figures 7 & 8. Figure 11 displays various types of cylindrical micellar filaments with different bending rigidities, such as thick bundles of micellar filaments, bundles of packed parallel straight filaments, distinct mixed micellar filaments with curvilinear centrelines, and distinct parallel filaments with curvilinear centrelines. The flexural rigidity EI takes different values for these topologies, depending on their elastic modulus E and diameter 2ξ. In samples of similar geometries such as the ones in Figure 11_b and Figure 11_d, the sample with a higher value of elastic modulus E tends to be straight, whereas the sample with lower value of E adopts a curvilinear geometry. According to Gohy *et al.*,[72] cylindrical micellar filaments tend to form bundles of closely-packed parallel filaments in the dehydrated state (Figure 11_b). This arrangement has not been detected in micellar solutions by light scattering technique, and thus appears to be formed during the dehydration process.

The elastic modulus of micellar filaments can be determined using different experiments such as indentation test, and the three-point bending test. Here, AFM was used to measure the elastic modulus E of a sample of micellar filaments through the indentation test. The elastic modulus was evaluated using the Hertzian contact mechanics model. Figure 12_a displays the distribution

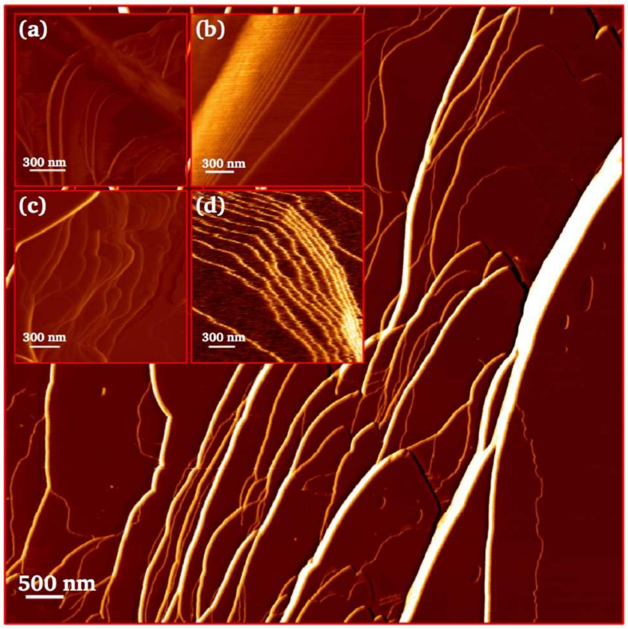

Fig. 11 Contact mode AFM images of micellar filaments in a semi-dilute solution, obtained in the dehydrated state at room temperature; (a), (b), (c), & (d) exhibit, respectively, thick bundles of cylindrical micellar filaments, bundles of packed parallel straight filaments, distinct mixed micellar filaments with curvilinear centrelines, and distinct parallel filaments with curvilinear centrelines.

of the measured elastic modulus from different cylindrical micellar filaments in a dehydrated state. The red rectangular columns show the histogram of the experimental data, and the solid line is an exponential fit to the data. Figure 12_b shows an AFM height image of an example of a created force map with a few selected spots for indentation on a cylindrical micellar filament. The black dots represent the selected positions in which the indentation was performed. In a dehydrated state, the elastic modulus of filaments was found to be $\approx 0.863 \pm 0.316$ MPa. The nano-indentation test was also performed on end caps to investigate the elastic modulus at those points (Figure 12_d). Consistent with previous observations, the elastic modulus, and consequently, the elastic bending energy at the end points of the filaments were found to be at least one order of magnitude higher than those within the cylindrical body. This contribution is crucial in determining the final topology of the filaments in micellar solutions at different concentrations, and explains the tendency of the micelles to grow in a semi-dilute solution, in order to reduce the number of end caps and reach the minimum elastic bending energy at equilibrium. The energy required to create two end caps from a very long cylindrical micellar filament is known as the scission energy. This energy is large relative to the elastic bending energy of the micellar body. For this reason, when the total surfactant volume fraction is relatively low, the semi-flexible cylindrical micellar filaments may elongate and become entangled with each other in order to reduce scission energy. The topology of micellar filaments is essentially determined by the balance between the conformational entropy, the elastic free energy of the micellar body, and most importantly, the excess energy coming from the end caps of open filaments. Our results indicate that semi-flexible linear micelles have a relatively large local strain energy at their end points, which explains their tendency to fuse to minimize the number of end caps. Detailed studies investigating the elastic properties of micellar filaments, with associated mechanical tests, will be the subject of future research.

To apply the Hertzian contact model, the strains are assumed to be infinitesimal and below the elastic limit. Up to an admissible approximation, this condition is satisfied in our experiments. The indentation depth ($\approx$5–10 nm) is selected to be small to avoid the effects of the substrate and also nonlinear or inelastic material behaviour in higher strains. Further, the indentation depth is selected to be much smaller than the radius of the indenting sphere and the diameter of the filaments. Considering the small diameter of micellar filaments, an indentation depth of 5 nm or less would have been ideal to measure their elastic modulus. However, since such filaments are very soft, selecting a low indentation depth would lead to an increase in the signal-to-noise ratio. Thus, limiting the indentation depth to 5 nm or less may yield results that are indicative of surface properties of the filament rather than the bulk properties of the filaments. A large indentation depth, however, might cause the indentation results to be influenced by the underlying mica substrate and thus the stiffness of micellar filaments could be slightly overestimated.

Table 1 The measured dynamic elastic modulus E of micellar filaments for different values of indentation frequency $\tilde{\omega}$.

t_e & t_r (ms)	Indentation frequency (Hz)	Analyzed points	Elastic modulus (MPa)
500	1	16159	0.863 ± 0.316
100	5	15441	0.983 ± 0.279
50	10	16133	1.132 ± 0.383
20	25	16231	1.818 ± 0.422
10	50	14223	2.662 ± 0.537
5	100	15372	3.409 ± 0.407
2.5	200	16083	3.972 ± 0.623

To investigate the effect of indentation frequency on the elastic behaviour of micellar filaments, additional nano-indentation tests were performed at different frequencies of 1–200 Hz. The extend time t_e and retract time t_r in indentation tests were set to be equal at each frequency. The measured dynamic elastic modulus E of micellar filaments for different values of indentation frequency $\tilde{\omega} = 1/(t_e + t_r)$ from 1 to 200 Hz, is expressed as the mean $\pm$ standard deviation in Table 1.

The indentation frequency was found to directly influence the measured elastic modulus of micellar filaments. The elastic modulus of the filaments obtained at 200 Hz was found to be greater than the one obtained at 1 Hz. This finding explains the different elastic behaviours that we observe at different loading rates in a quantitative way. Further, for the same indenting force, the indentation depth was found to decrease as the loading rate increased from 1 to 200 Hz. This observation suggests that micellar filaments, like many other bio-filaments, show a higher elastic modulus at higher loading rates. The increase in elastic modulus at higher frequencies can be regarded as a consequence of

View Article Online
DOI: 10.1039/C7SM00911A

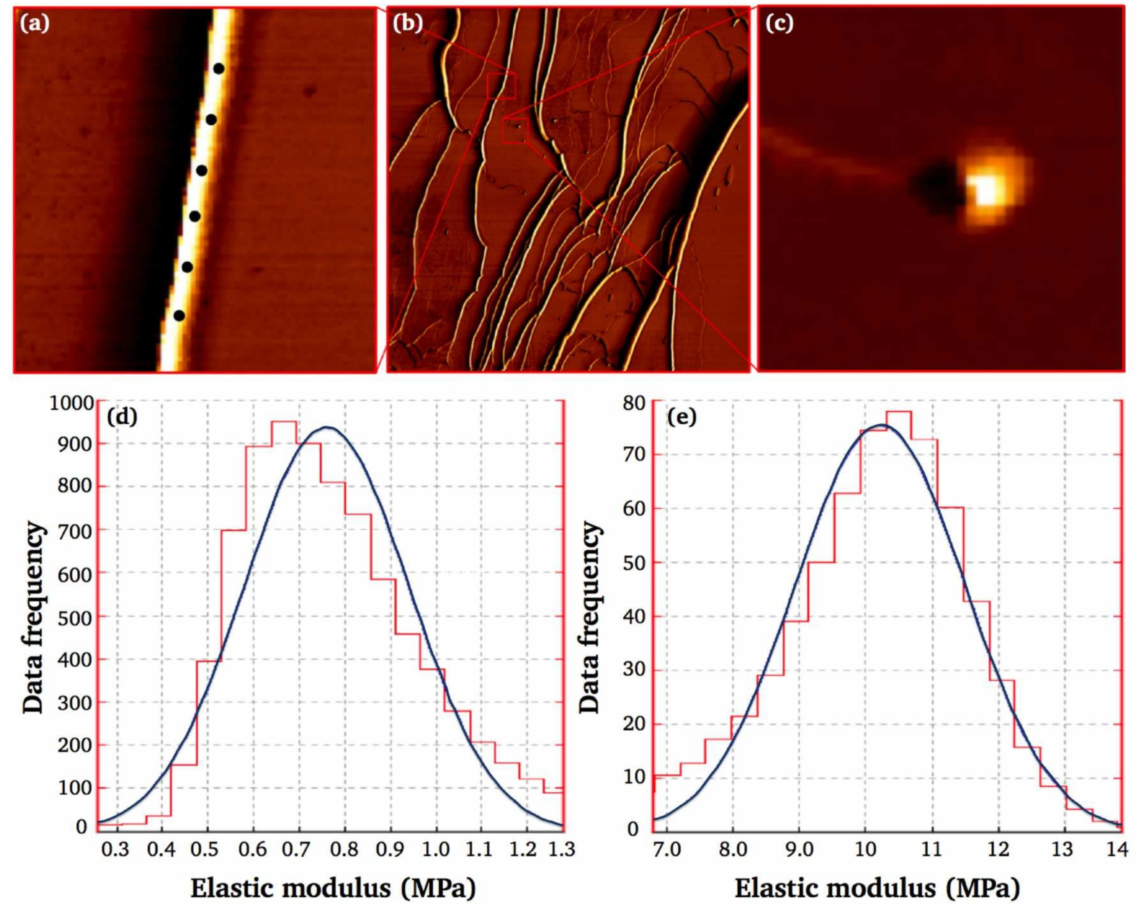

Fig. 12 Representative indentation results; (a) AFM height image of an example of a created force map with a few selected spots for indentation on a cylindrical micellar filament. The black dots represent the selected positions in which the indentation was performed; (b) AFM image of a network of bundles of cylindrical micellar filaments in the dehydrated state at room temperature; (c) Image of an end cap indented in the dehydrated state; (d) Graph of the distribution of the measured elastic modulus from different cylindrical micellar filaments in the dehydrated state. The red rectangular columns represent the histogram of the experimental data, and the solid line is an exponential fit to the data; (e) Distribution of the measured elastic modulus at end caps. In the dehydrated state, the elastic modulus of filaments was found to be $\approx 0.863 \pm 0.316$ MPa. Also, our results indicate that the elastic modulus of the filament at end caps ($\approx 10.541 \pm 3.622$ MPa) is at least one order of magnitude higher than that within the cylindrical body.

the viscoelasticity of micellar filaments. Our results are coherent with most of the previous studies that report the *bulk* shear modulus $G \approx E/3$ of CTAB/NaSal micellar solutions increasing when the angular frequency of rheometer increases from 0.01 to 100 Hz.[23,73,74] Nevertheless, the *value* of the elastic modulus of single micellar filaments obtained using nano-indentation cannot be compared with the elastic properties of the *bulk solution* obtained using rheometry.

The Gaussian regression functions in our indentation analysis of individual micellar filaments in a dehydrated state reaches a maximum at 0.863 ± 0.316 MPa for the elastic modulus E at the loading rate of 1 Hz. Indentation measurements on the same sample at the loading rate of 200 Hz yield a larger elastic modulus ranging from ≈ 3–5 MPa with a peak at 3.972 ± 0.623 MPa. Statistically significant differences were found between the elastic moduli at 1 and 200 Hz. Our results indicate a good correspondence with most of the previously obtained values of the elastic modulus and flexural rigidity for micellar filaments in the dehydrated state.[23,67,77–79] However, like other bio-filaments, elastic moduli of the dehydrated samples of micellar filaments are expected to be at least a few orders of magnitude larger than those of the hydrated ones.[45] The obtained value of 0.863 ± 0.316 MPa for the elastic modulus E yields the persistence length $\langle l_p \rangle$ of $\approx$10–200 nm for micellar filaments of different radii. This value for the persistence length is on the same order as previously reported values for CTAB-based micellar solutions.[77,80,81] It should be noted that various factors influence the elastic modulus of micelles. For instance, previous experimental observations have indicated that adding salt significantly increases the mechanical stiffness of micellar filaments.[76] Here we used specific concentrations of NaSal/CTAB. Detailed investigation of the effect of salt concentration on micellar elastic modulus are considered as a subject for future research.

Previous studies on other bio-filaments have reported that dehydration can result in a large increase, up to a few orders of magnitude, in the elastic modulus of such filaments.[45] Those studies argue that the modulus of bio-filaments reaches a plateau in frequencies as low as 1 Hz. However, such an equilibrium state may not be reached in high loading rates. Detailed studies of viscoelastic properties of micellar filaments and associated mechanical models are also a subject for future research.

7 Concluding remarks

Although experiments reveal many geometric features of micellar filaments, theoretical modeling is required to expand our understanding of these observed experimental systems, and to provide predictive tools for the kinetic features in similar studies. In the present study, the previously developed micro-mechanical model for the elasticity of micellar filaments was extended to obtain the elastic bending energy of the hemispherical end caps in open cylindrical micellar filaments. The resulting bending energy at each end cap was found to incorporate quadratic terms in curvature and torsion at that point as well as a homogeneous contribution. This term was found to be insensitive to the shape of the end cap, and may have implicit dependence upon effects like temperature, concentration, and electromagnetic fields.

We then applied constrained Cosserat rod theory to obtain the macroscopic elastic bending energy of such nanostructures. While the continuum mechanical approach provides macroscopic description of a micellar filament, the micro-mechanical approach has a microscopic view of that medium, and provides expressions for kinetic variables such as forces based on a selected interaction potential between the molecules comprising the filament. Their different natures notwithstanding, these two perspectives provide complementary and consistent information when applied to the same physical problem. As in the micro-mechanical model, in the continuum mechanical model the elastic bending energy density of the filament was found to be quadratic in the curvature of the centreline. However, unlike the micro-mechanical model, the continuum description of the elastic bending energy of the filament was found to incorporate the twisting density rather than the torsion of the centreline. In other words, we found that continuum mechanical model includes the relative rotation of the material line elements within the cross-section.

Unlike the continuum mechanical model, the micro-mechanical model yields integral representations for elastic modulus as well as flexural and torsional rigidities in terms of the molecular interactions, molecular distribution function, and molecular dimensions. By applying an anisotropic Gaussian potential in the micro-mechanical model, the elastic moduli of the filament were obtained in terms of the density of the molecules and their dimensions. Consistent with previous experimental observations, our micro-mechanical model predicted a monotonic increase in the local flexural rigidity of micellar filaments when the molecular aspect ratio increases. Further, the elastic modulus of the micellar filament was found to depend on the size of its constituent molecules.

Finally, Atomic Force Microscopy was used to perform the indentation test to measure the local elastic modulus of the filaments on the micellar body and at the end points at the indentation frequency of 1 Hz. Our results indicated that the elastic modulus of the filament at the end caps ($\approx 10.541 \pm 3.622$ MPa) is at least one order of magnitude higher than that within the cylindrical body ($\approx 0.863 \pm 0.316$ MPa). This finding indicates that semi-flexible linear micelles have a relatively large local strain energy at their end points, which might explain their tendency to fuse to minimize the number of end caps. The effect of indentation frequency on the elastic modulus of micellar filaments was also investigated. Indentation tests were performed at frequencies as high as 200 Hz. Consistent with previous experimental observations on the *bulk* shear modulus of micellar *solutions*, it was found that the elastic modulus of a single micellar filament at high loading rates is larger than that at low frequencies.

8 Acknowledgements

Support from the National Institutes of Health (NIDCD grant R01-DC005788) and the Canadian Foundation for Innovation (CFI grant 229251) is gratefully acknowledged. The author thanks Professors L. Mongeau and H. Vali at McGill University for granting access to their laboratory instruments, Neda Latifi and Rachel Price for constructive comments, and Sophia Hohlbauch and Ernesto Lopez for helpful hints about AFM. Various helpful comments by Professor Jeff Z. Y. Chen from the Department of Physics and Astronomy at the University of Waterloo are gratefully acknowledged.

9 Appendices

9.1 Expansion of the end cap energy

Here we present the expansion of (10) in powers of ε to obtain (12). Using Eqs. (A.3) in Ref.[21] and the definition $t_1 = t_\circ + s\varepsilon$, the four arguments of the interaction potential in (7) are obtained in terms of the arc-length s and the dimensionless parameter ε as[21,47]

$$\varepsilon^{-2}|\boldsymbol{\chi}(t_\circ) - \boldsymbol{\chi}(t_1)|^2 = s^2 + \mathbb{B}_1 \varepsilon^2 s^4 + o(\varepsilon^2),$$

$$\big\langle \boldsymbol{\chi}(t_\circ) - \boldsymbol{\chi}(t_1) \big\rangle \cdot \mathbf{d}(t_\circ, \theta) = \mathbb{B}_2 \varepsilon^2 s^2 + o(\varepsilon^2),$$

$$\big\langle \boldsymbol{\chi}(t_\circ) - \boldsymbol{\chi}(t_1) \big\rangle \cdot \mathbf{d}(t_1, \eta) = \mathbb{B}_3 \varepsilon^2 s^2 + o(\varepsilon^2),$$

$$\big\langle \mathbf{d}(t_\circ, \theta) \cdot \mathbf{d}(t_1, \eta) \big\rangle = \mathbb{B}_\circ + \mathbb{B}_4 \varepsilon s + \mathbb{B}_5 \varepsilon^2 s^2 + o(\varepsilon^2), \tag{37}$$

where $\mathbb{B}_\circ = \cos(\theta - \eta)$, $\mathbb{B}_1 = -\kappa^2/12$, $\mathbb{B}_2 = -\kappa \cos\theta/2$, $\mathbb{B}_3 = \kappa \cos\eta/2$, $\mathbb{B}_4 = \tau \sin(\theta - \eta)$ and $2\mathbb{B}_5 = \dot{\tau} \sin(\theta - \eta) + 4\mathbb{B}_2\mathbb{B}_3 - \tau^2 \mathbb{B}_\circ$. Let $\mathscr{E}_c(\theta, \phi)$ in (10) be replaced from (11). Using the expansions (37) while replacing $\mathscr{E}_c(\theta, \phi)$ from (7), and performing the change of variables $L - t_\circ = \varepsilon s$ (neglecting terms proportional to ε^3 and higher), the right-hand side of (10) takes the form

$$\bar{\psi}^{\text{cap}} = \varepsilon \int_0^{L/\varepsilon} \int_0^{2\pi} \int_0^{2\pi} \int_0^{\frac{\pi}{2}} \tilde{\Omega}\Big(\varepsilon^{-2} |\tilde{\mathbf{r}}(s)|^2, \tilde{\mathbf{r}}(s) \cdot \mathbf{e}(\theta, \phi), \tilde{\mathbf{r}}(s) \cdot \mathbf{d}(s, \eta),$$

$$\mathbf{e}(\theta, \phi) \cdot \mathbf{d}(s, \eta) \Big) \mathscr{D}_e \mathscr{D}(L - s\varepsilon) \, \mathrm{d}\phi \, \mathrm{d}\theta \, \mathrm{d}\eta \, \mathrm{d}s, \tag{38}$$

where $\tilde{\mathbf{r}}(s) = \boldsymbol{\chi}(L) - \boldsymbol{\chi}(L - s\varepsilon)$. Applying the Taylor expansion for $\tilde{\Omega}$ and $\mathscr{D}$ in (38) results in

$$\bar{\psi}^{\text{cap}} = \bar{\psi}_\circ + \bar{k}_c^{\text{cap}} \kappa_c^2 + \bar{k}_t^{\text{cap}} \tau_c^2, \tag{39}$$

in which

$$\bar{\psi}_\circ = \varepsilon \int_0^{\ell}\int_0^{2\pi}\int_0^{2\pi}\int_0^{\frac{\pi}{2}} \Bigg(\bar{\Omega}(s)\mathscr{D}_e\Big(\mathscr{D}(s)+\dot{\mathscr{D}}(s)\varepsilon s+\ddot{\mathscr{D}}(s)\frac{\varepsilon^2 s^2}{2}\Big)$$

$$-\bar{\Omega}_2(s,\theta,\phi,\eta)\cos\phi\,\mathscr{D}_e\Big(\mathscr{D}(s)\varepsilon s+\dot{\mathscr{D}}(s)\varepsilon^2 s^2\Big)$$

$$+\bar{\Omega}_{22}(s,\theta,\phi,\eta)\cos^2\phi\,\mathscr{D}_e\mathscr{D}(s)\varepsilon^2 s^2\Bigg)\,\mathrm{d}\phi\,\mathrm{d}\theta\,\mathrm{d}\eta\,\mathrm{d}s,$$

$$\bar{k}_t^{\mathrm{cap}} = \frac{-\varepsilon^3}{2}\int_0^{\ell}\int_0^{2\pi}\int_0^{2\pi}\int_0^{\frac{\pi}{2}} \mathscr{D}_e\mathscr{D}(s)s^2\sin\phi\,\Big(\cos(\theta-\eta)\bar{\Omega}_4(s,\theta,\phi,\eta)$$

$$-\sin^2(\theta-\eta)\sin\phi\;\bar{\Omega}_{44}(s,\theta,\phi,\eta)\Big)\,\mathrm{d}\phi\,\mathrm{d}\theta\,\mathrm{d}\eta\,\mathrm{d}s,$$

$$\bar{k}_c^{\mathrm{cap}} = \frac{\varepsilon^3}{2}\int_0^{\ell}\int_0^{2\pi}\int_0^{2\pi}\int_0^{\frac{\pi}{2}} -\mathscr{D}_e\mathscr{D}(s)s^2\Big(\frac{s^2}{6}\bar{\Omega}_1(s,\theta,\phi,\eta)$$

$$+\sin\phi\cos\theta\cos\eta\,\bar{\Omega}_4(s,\theta,\phi,\eta)\Big)\,\mathrm{d}\phi\,\mathrm{d}\theta\,\mathrm{d}\eta\,\mathrm{d}s, \tag{40}$$

where $\bar{\Omega}(s,\theta,\phi,\eta) := \tilde{\Omega}(s^2,0,0,\beta)$, $\bar{\Omega}_{,i}(s,\theta,\phi,\eta) := \tilde{\Omega}_{,i}(s^2,0,0,\beta)$, $\bar{\Omega}_{,ii}(s,\theta,\phi,\eta) := \tilde{\Omega}_{,ii}(s^2,0,0,\beta)$, and $\beta = \sin\phi\,\cos(\theta-\eta)$ for $i \in \{1,2,3,4\}$.

9.2 Integral representations in Eq. (35)

$$\mathscr{I}_1 = \int_0^{2\pi}\int_0^{2\pi}\int_0^{\frac{\pi}{2}} \frac{1}{\sqrt{1-\chi^2\cos^2(\theta-\eta)\sin^2\phi}}\,\mathrm{d}\phi\,\mathrm{d}\theta\,\mathrm{d}\eta,$$

$$\mathscr{I}_2 = \int_0^{2\pi}\int_0^{2\pi}\int_0^{\frac{\pi}{2}} \frac{\cos^2(\theta-\eta)\sin^2\phi}{\sqrt{1-\chi^2\cos^2(\theta-\eta)\sin^2\phi}}\,\mathrm{d}\phi\,\mathrm{d}\theta\,\mathrm{d}\eta,$$

$$\mathscr{I}_3 = \int_0^{2\pi}\int_0^{2\pi}\int_0^{\frac{\pi}{2}} \frac{\cos\eta\cos\theta\cos(\theta-\eta)\sin^2\phi}{\sqrt{1-\chi^2\cos^2(\theta-\eta)\sin^2\phi}}\,\mathrm{d}\phi\,\mathrm{d}\theta\,\mathrm{d}\eta. \tag{41}$$

9.3 Integral representations in Eq. (36)

$$\mathscr{J}_1 = \int_0^{2\pi}\int_0^{2\pi}\int_0^{\frac{\pi}{2}} \frac{\cos^2\phi\sqrt{1-\chi^2\cos^2(\theta-\eta)\sin^2\phi}}{1-\chi\cos(\theta-\eta)\sin\phi}\,\mathrm{d}\phi\,\mathrm{d}\theta\,\mathrm{d}\eta,$$

$$\mathscr{J}_2 = \int_0^{2\pi}\int_0^{2\pi}\int_0^{\frac{\pi}{2}} \frac{\cos^2\phi\sqrt{1-\chi^2\cos^2(\theta-\eta)\sin^2\phi}}{1+\chi\cos(\theta-\eta)\sin\phi}\,\mathrm{d}\phi\,\mathrm{d}\theta\,\mathrm{d}\eta,$$

$$\mathscr{J}_3 = \int_0^{2\pi}\int_0^{2\pi}\int_0^{\frac{\pi}{2}} \frac{\cos^2\phi\sqrt{1-\chi^2\cos^2(\theta-\eta)\sin^2\phi}}{\chi'\cos(\theta-\eta)\sin\phi+1}\,\mathrm{d}\phi\,\mathrm{d}\theta\,\mathrm{d}\eta,$$

$$\mathscr{J}_4 = \int_0^{2\pi}\int_0^{2\pi}\int_0^{\frac{\pi}{2}} \frac{\cos^2\phi\sqrt{1-\chi^2\cos^2(\theta-\eta)\sin^2\phi}}{\chi'\cos(\theta-\eta)\sin\phi-1}\,\mathrm{d}\phi\,\mathrm{d}\theta\,\mathrm{d}\eta,$$

$$\mathscr{J}_5 = \int_0^{2\pi}\int_0^{2\pi}\int_0^{\frac{\pi}{2}} \sqrt{1-\chi^2\cos^2(\theta-\eta)\sin^2\phi}\,\mathrm{d}\phi\,\mathrm{d}\theta\,\mathrm{d}\eta. \tag{42}$$

References

1 J. N. Israelachvili, *Intermolecular and surface forces: revised third edition,* Academic press, 2011.
2 J. N. Israelachvili, D. J. Mitchell, B. W. Ninham, *J. Chem. Soc., Faraday Trans. 2,* 1976, **72**, 1525–1568.
3 M. E. Cates, S. J. Candau, *J. Phys. Condens. Matter,* 1990, **2**, 6869–6892.
4 M. E. Cates, M. S. Turner, *Europhys. Lett.,* 1990, **11**, 681–686.
5 N. A. Spenley, M. E. Cates, T. C. B. McLeish, *Phys. Rev. Lett.*, 1993, **71**, 939.
6 L. Jiang, K. Wang, M. Deng, Y. Wang, J. Huang, *Langmuir*, 2008, **24**, 2825–2835.
7 A. Wang, W. Shi, J. Huang, Y. Yan, *Soft Matter*, 2016, **12**, 337–357.
8 B. M. Discher, Y. Y. Won, D. S. Ege, J. C. M. Lee, F. S. Bates, D. E. Discher, D. A. Hammer, *Science*, 1999, **284-5417**, 1143–1146.
9 H. Cui, Z. Chen, S. Zhong, K. L. Wooley, D. J. Pochan, *Science*, 2007, **317-5838**, 647–650.
10 C. A. Dreiss, *Soft Matter*, 2007, **3**, 956–970.
11 C. Oelschlaeger, M. Schopferer, F. Scheffold, N. Willenbacher, *Langmuir*, 2008, **25**, 716–723.
12 S. Zhong, H. Cui, Z. Chen, K. L. Wooley, D. J. Pochan, *Soft Matter*, 2008, **4**, 90–93.
13 A. Bernheim-Groswasser, R. Zana, Y. Talmon, *J. Phys. Chem. B*, 2000, **104**, 4005–4009.
14 G. Porte, R. Gomati, O. E. Haitamy, J. Appell, J. Marignan, *J. Phys. Chem.*, 1986, **90**, 5746–5751.
15 L. van Dam, G. Karlsson, K. Edwards, *Biochim. Biophys. Acta*, 2004, **1664**, 241–256.
16 S. May, Y. Bohbot, A. Ben-Shaul, *J. Phys. Chem. B*, 1997, **101**, 8648–8657.
17 R. Zana, E. W. Kaler, *Giant micelles: properties and applications,* CRC Press, 2007.
18 Z. Lin, J. J. Cai, L. E. Scriven, H. T. Davis, *J. Phys. Chem.* **1994**, *98*, 5984–5993.
19 S. Dhakal, R. Sureshkumar, *J. Chem. Phys.*, 2015, **143**, 024905.
20 F. C. MacKintosh, S. A. Safran, P. A. Pincus, *Europhys. Lett.*, 1990, **12**, 697.
21 M. Asgari, *Eur. Phys. J. E Soft Matter,* 2015, **38**, 1–16.
22 F. Nettesheim, N. J. Wagner, *Langmuir*, 2007, **23**, 5267–5269.
23 B. A. Schubert, E. W. Kaler, N. J. Wagner, *Langmuir*, 2003, **19**, 4079–4089.
24 E. S. Boek, J. T. Padding, W. K. den Otter, W. J. Briels,*J. Phys. Chem. B*, 2005, **109**, 19851–19858.
25 P. B. Canham, *J. Theor. Biol.*, 1970, **26**, 61–81.
26 W. Helfrich, *Z. Naturforsch.*, 1973, **28**, 693.
27 D. J. Steigmann, *Arch. Ration. Mech. Anal.*, 1999, **150(2)**, 127–152.
28 M. Tang, W. C. Carter, *J. Phys. Chem. B*, 2013, **117**, 2898–2905.
29 Z. Li, Z. Chen, H. Cui, K. Hales, K. L. Wooley, D. J. Pochan, *Langmuir*, 2007, **23**, 4689–4694.
30 J.-F. Berret, *Molecular gels*, 2006, 667–720.
31 V. A. Andreev, A. I. Victorov, *Mol. Phys.*, 2007, **105**, 239–247.

View Article Online
DOI: 10.1039/C7SM00911A

32 N. Saitô, K. Takahashi, Y. Yunoki, *J. Phys. Soc. Jpn.*, 1967, **22**, 219–226.

33 P. G. De Gennes, *Scaling concepts in polymer physics, Cornell university press*, 1979.

34 Y. Lauw, F. A. M. Leermakers, M. A. Cohen Stuart *J. Phys. Chem. B*, 2003, **107**, 10912–10918.

35 L. M. Walker, *Curr. Opin. Colloid Interface Sci.*, 2001, **6**, 451–456.

36 L. M. Bergström, *Langmuir*, 2009, **25**, 1949–1960.

37 Y. Liu, T. Pérez, W. Li, J. D. Gunton, A. Green, *J. Chem. Phys.*, 2011, **134**, 065107-1–6.

38 O. Kratky, G. Porod, *Recl. Trav. Chim. Pays-Bas*, 1949, **68**, 1106–1122.

39 P. Bugl, S. Fujita, *J. Chem. Phys.*, 2003, **50**, 3137–3142.

40 W. Helfrich, *Langmuir*, 1991, **7**, 567–568.

41 M. In, O. Aguerre-Chariol, R. Zana, *J. Phys. Chem. B*, 1999, **103**, 7747–7750.

42 S. May, A. Ben-Shaul, *J. Phys. Chem. B*, 2001, **105**, 630–640.

43 M. B. Rubin, *Cosserat theories: shells, rods and point, Kluwer, Dordrecht,* 2000.

44 E. Cosserat, F. Cosserat, *Paris*, 1909, **3**, 17–29.

45 M. Asgari, N. Latifi, H. K. Heris, H. Vali, L. Mongeau, *Sci. Rep.*, 2017, **7**, DOI: 10.1038/s41598-017-01476-y.

46 I. LaRue, A. Adam, M. Da Silva, S. S. Sheiko, M. Rubinstein, *Macromolecules*, 2004, **37**, 5002–5005.

47 M. Asgari, A. Biria, *Int. J. Nonl. Mech.*, 2015, **76**, 135–143.

48 T. Shikata, S. J. Dahman, D. S. Pearson, *Langmuir*, 1994, **10**, 3470–3476.

49 D. J. Struik, *Lectures on classical differential geometry,* Dover, New York, 1961.

50 S. Jain, F. S. Bates, *Science*, 2003, **300**, 460–464.

51 J. B. Keller, G. J. Merchant, *J. Stat. Phys.*, 1991, **63**, 1039–1051.

52 C. Truesdell, W. Noll, *The non-linear field theories of mechanics,* Springer, 2004.

53 S. de Prado, P. González, M. Encinar, A. Alonso, M. Vélez, P. Tarazona, *Chem. Phys. Lipids,* 2015, **185**, 141–152.

54 L. D. Landau, E. M. Lifshitz, *Elasticity theory,* Pergamon press, 1975.

55 Y. Liu, T. Pérez, W. Li, J. D. Gunton, A. Green, *J. Chem. Phys.*, 2011, **134**, 065107.

56 P. G. de Prado Salas, I. Hörger, F. Martín-García, J. Mendieta, Á. Alonso, M. Encinar, P. Gómez-Puertas, M. Vélez, P. Tarazona, *Soft matter*, 2014, **10**, 1977–1986.

57 M. E. Helgeson, T. K. Hodgdon, E. W. Kaler, N. J. Wagner, *J. Colloid Interface Sci.*, 2010, **349**, 1–12.

58 J. F. Marko, E. D. Siggia, *Macromolecules*, 1994, **27**, 981–988.

59 A. Balaeff, L. Mahadevan, K. Schulten, *Phys. Rev. E*, 2006, **73**, 031919.

60 B. J. Berne, P. Pechukas, *J.* Chem. Phys., 2003, **56**, 4213.

61 J. G. Gay, B. J. Berne, *J.* Chem. Phys., 1981, **74**, 3316.

62 L. Whitehead, C. M. Edge, J. W. Essex, *J. Comput. Chem.*, 2001, **22**, 1622.

63 J. E. Marsden, T. J. Hughes, *Mathematical foundations of elasticity,* Courier Corporation, 1994.

64 S. S. Antman, *Nonlinear problems of elasticity,* Springer, New York, 2005.

65 D. J. Steigmann, *Int. J. Nonl. Mech.*, 2012, **47**, 734–742.

66 E. L. Starostin, G. H. M. van Der Heijden, *Phys. Rev. E*, 2009, **79**, 066602.

67 L. Jennings, P. Glazer, A. C. Laan, R. M. de Kruijff, G. Waton, F. Schosseler, E. Mendes, *Soft matter*, 2016, **12**, 7324–7329.

68 G. H. M. van der Heijden, *Proc. R. Soc. Lond. A*, 2001, **457**, 695–715.

69 S. P. Timoshenko, *Strength of materials*, D. van Nostrand, 1956.

70 J. J. Cardiel, H. Furusho, U. Skoglund, A. Q. Shen, *Sci. Rep.*, 2015, **5**.

71 A. Goriely, M. Tabor, *Physica D: Nonlinear Phenomena*, 1997, **105**, 20–44.

72 J. F. Gohy, B. Lohmeijer, A. Alexeev, X. Wang, I. Manners, M. A. Winnik, U. S. Schubert, *Chem. Eur. J.*, 2004, **10**, 4315–4323.

73 J. J. Cardiel, A. C. Dohnalkova, N. Dubash, Y. Perry, A. Q. Shen, *Proc. Natl. Acad. Sci.*, 2013, **110**, 1653–1660.

74 N. Dubash, J. J. Cardiel, P. Cheung, A. Q. Shen, *Soft Matter*, 2011, **7**, 876–879.

75 Z. Wang, F. Sun, S. Huang, C. Yan, *J. Polym. Sci. Part B Polym. Phys.*, 2016, **54**, 1450–1457.

76 Y. Geng, F. Ahmed, N. Bhasin, D. E. Discher, *J. Phys. Chem. B*, 2005, **109**, 3772–3779.

77 L. J. Magid, Z. Li, P. D. Butler, *Langmuir*, 2000, **16**, 10028–10036.

78 P. Dalhaimer, F. S. Bates, D. E. Discher, *Macromolecules*, 2003, **36**, 6873–6877.

79 Y. I. Rabinovich, I. U. Vakarelski, S. C. Brown, P. K. Singh, B. M. Moudgil, *J. Colloid Interface Sci.*, 2004, **2**70, 29–36.

80 W. R. Chen, P. D. Butler, L. J. Magid, *Langmuir*, 2006, **2**2, 6539–6548.

81 C. Oelschlaeger, P. Suwita, N. Willenbacher, *Langmuir*, 2010, **2**6, 7045–7053.

82 O. Abillon, E. Perez, *J. Phys. France*, 1990, **5**1, 2543–2556.

83 H. Jung, B. Coldren, J. Zasadzinski, D. Iampietro, E. Kaler, *Proc. Natl. Acad. Sci.*, 2001, **9**8, 1353–1357.